

AMAZE. I. The evolution of the mass–metallicity relation at $z>3$ [★]

R. Maiolino¹, T. Nagao², A. Grazian¹, F. Cocchia¹, A. Marconi³, F. Mannucci⁴, A. Cimatti⁵, A. Pipino⁶, S. Ballero⁷,
F. Calura⁷, C. Chiappini^{10,11}, A. Fontana¹, G.L. Granato⁸, F. Matteucci⁷, G. Pastorini³, L. Pentericci¹, G. Risaliti⁹,
M. Salvati⁹, and L. Silva¹⁰

- ¹ INAF - Osservatorio Astronomico di Roma, via di Frascati 33, 00040 Monte Porzio Catone, Italy
² National Astronomical Observatory of Japan, 2-21-1 Osawa, Mitaka, Tokyo 181-8588, Japan
³ Dipartimento di Astronomia, Università di Firenze, Largo E. Fermi 2, 50125 Firenze, Italy
⁴ INAF - Istituto di Radioastronomia, Largo E. Fermi 5, 50125 Firenze, Italy
⁵ Dipartimento di Astronomia, Università di Bologna, via Ranzani 1, 40127, Bologna, Italy
⁶ Astrophysics, University of Oxford, Keble Road, Oxford OX1 3RH, United Kingdom
⁷ Dipartimento di Astronomia, Università di Trieste, via Tiepolo 11, 34131 Trieste, Italy
⁸ INAF - Osservatorio Astronomico di Padova, Vicolo Osservatorio 5, 35122 Padova, Italy
⁹ INAF - Osservatorio Astrofisico di Arcetri, Largo E. Fermi 5, 50125 Firenze, Italy
¹⁰ INAF - Osservatorio Astronomico di Trieste, Via Tiepolo 11, 34131 Trieste, Italy
¹¹ Geneva Observatory, Geneva University, 51 chemins des Mailletes, CH 1290, Sauverny, Switzerland

Received ; accepted

ABSTRACT

We present initial results of an ESO-VLT large programme (AMAZE) aimed at determining the evolution of the mass-metallicity relation at $z>3$ by means of deep near-IR spectroscopy. Gas metallicities are measured, for an initial sample of nine star forming galaxies at $z\sim 3.5$, by means of optical nebular lines redshifted into the near-IR. Stellar masses are accurately determined by using Spitzer-IRAC data, which sample the rest-frame near-IR stellar light in these distant galaxies. When compared with previous surveys, the mass-metallicity relation inferred at $z\sim 3.5$ shows an evolution much stronger than observed at lower redshifts. The evolution is prominent even in massive galaxies, indicating that $z\sim 3$ is an epoch of major action in terms of star formation and metal enrichment also for massive systems. There are also indications that the metallicity evolution of low mass galaxies is stronger relative to high mass systems, an effect which can be considered the chemical version of the galaxy downsizing. The mass-metallicity relation observed at $z\sim 3.5$ is difficult to reconcile with the predictions of some hierarchical evolutionary models. Such discrepancies suggest that at $z>3$ galaxies are assembled mostly with relatively un-evolved sub-units, i.e. small galaxies with low star formation efficiency. The bulk of the star formation and metallicity evolution probably occurs once small galaxies are already assembled into bigger systems.

Key words. ISM: abundances – galaxies: abundances – galaxies: evolution – galaxies: high-redshift – galaxies: starburst

1. Introduction

The connection between galaxy mass and metallicity has been known for a long time, starting with the seminal work of Lequeux et al. (1979). Given the difficulty in obtaining reliable galaxy masses several authors have resorted in using the (optical) luminosity. In particular, various works have reported a clear correlation between blue luminosity and metallicity, in the sense that more luminous galaxies are characterized by higher metallicities (e.g. Garnett & Shields, 1987; Skillman et al., 1989; Brodie & Huchra, 1991; Zaritsky et al., 1994). A major step forward has been recently achieved by Tremonti et al. (2004), who used optical photometric and spectroscopic data of a sample of $\sim 53,000$ galaxies from the SDSS to determine the mass-metallicity relation of local galaxies ($z\sim 0.1$). Their work clearly showed that the primary physical parameter driving the correlation with the gas metallicity is the (stellar) mass of galaxies and not their luminosity. While Tremonti et al. (2004) focused on the gas metallicity, a similar relation by using the SDSS sur-

vey was found by Gallazzi et al. (2006) for what concerns the stellar metallicity.

Various physical processes may be responsible for the mass-metallicity relation. One possibility is that outflows, generated by starburst winds, eject metal-enriched gas into the IGM preferentially out of low-mass galaxies (due to the shallow gravitational potential well), making their enrichment less effective than in massive systems (e.g. Tremonti et al., 2004; De Lucia et al., 2004; Finlator & Davé, 2008). An alternative scenario is that low mass systems are still at an early evolutionary stage and have still to convert most of their gas into stars, hence they are poorly metal-enriched relative massive galaxies (which are instead already evolved). This is the so-called “galaxy downsizing” scenario, supported by various observational evidences (e.g. Juneau et al., 2005; Feulner et al., 2005; Franceschini et al., 2006; Asari et al., 2007; Perez-Gonzalez et al., 2007), where massive galaxies formed most of their stars rapidly and at high redshift, while low mass systems are characterized by a slower evolution, which extends to low redshift. Finally Köppen et al. (2007) ascribes the mass-metallicity relation to variations of the IMF high-mass cutoff in different star forming environments.

The relative role of these processes in shaping the mass-metallicity relation is debated. It is likely that each of them

Send offprint requests to: R. Maiolino

[★] Based on data obtained at the VLT through the ESO program 178.B-0838

contributes at least to some extent, since observational evidences have been found for all of them. Each of these factors (outflows/feedback, downsizing, IMF) has profound implications on the evolution of galaxies. Therefore, it is clear that the mass-metallicity relation contains a wealth of information useful to constrain models of galaxy formation and evolution. Indeed, any model of galaxy evolution is now required to match the mass–metallicity relation observed locally (e.g. Kobayashi et al., 2007; Brooks et al., 2007; de Rossi et al., 2007; Davé & Oppenheimer, 2007; Dalcanton, 2007; De Lucia et al., 2004; Tissera et al., 2005; Bouché et al., 2006, 2007; Köppen et al., 2007; Cid Fernandes et al., 2007; Finlator & Davé, 2008; Tassis et al., 2008). However, different models predict different evolutionary patterns of the mass-metallicity relation as a function of redshift, and observational data are required to test and discriminate among them.

Observational constraints of the mass-metallicity relation have been obtained up to $z\sim 2.2$ thanks to various deep surveys (Savaglio et al., 2005; Liang et al., 2006; Erb et al., 2006). Additional observational studies have investigated the evolution of the luminosity-metallicity relation or, more generally, the metallicity of high- z star forming galaxies (Kobulnicky & Koo, 2000; Kobulnicky et al., 2003; Kobulnicky & Kewley, 2004; Maier et al., 2004, 2005, 2006; Förster Schreiber et al., 2006). Note that all of these studies refer to the gas metallicity, while limited work has been done on the stellar metallicity of high redshift sources (Rix et al., 2004; de Mello et al., 2004; Halliday et al., 2008; Mehlert et al., 2006) due to difficulties in obtaining high S/N spectra on the stellar continuum. The general observational result is that the mass-metallicity relation (as well as the luminosity-metallicity relation) evolves, in the sense that on average higher redshift galaxies are characterized by lower metallicities (at a given mass). Whether the relation evolves also in terms of its shape is still matter of debate. Theoretical models can generally cope with the observed evolution, within both the theoretical and observational uncertainties (e.g. Kobayashi et al., 2007; de Rossi et al., 2007; Brooks et al., 2007; Finlator & Davé, 2008).

At $z\geq 3$, except for a few individual studies, little work has been currently done for what concerns the mass-metallicity relation. Pettini et al. (2001) have measured the metallicity for a small sample of Lyman Break Galaxies (LBG) at $z\sim 3$, but without investigating the mass-metallicity relation. The metallicity evolution has been investigated in DLA systems (Prochaska et al., 2003; Kulkarni et al., 2005; Akerman et al., 2005). However, a study of the mass-metallicity relation for high- z absorption systems has not been properly performed, due to difficulties in measuring the associated stellar masses. The closest result is the finding of a relation between metallicity and velocity dispersion (probably related to the mass) inferred by the width of the absorption systems (Ledoux et al., 2006; Prochaska et al., 2007).

We have undertaken a large observing programme at ESO-VLT aimed at carefully determining the mass-metallicity relation at $z>3$ for a sizeable sample of galaxies. The final goal is to obtain a detailed description of the evolution of the mass-metallicity evolution through the cosmic epochs, and therefore constrain galaxy evolutionary scenarios. In this paper we present preliminary results obtained by such a program, and discuss the relevant implications for our understanding of the galaxy evolution at high redshift. Throughout the paper we adopt the following cosmological parameters: $H_0 = 71 \text{ km s}^{-1} \text{ Mpc}^{-1}$, $\Omega_\Lambda = 0.73$ and $\Omega_m = 0.27$ (Spergel et al., 2003).

2. The AMAZE program

AMAZE (Assessing the Mass-Abundance redshift-[Z] Evolution) is an ESO large program aimed at determining the mass-metallicity relation in the redshift range $3<z<5$. Observations are being performed with SINFONI (Eisenhauer et al., 2003), the near-IR integral field spectrometer at VLT, for a total of 180 hours, distributed in three semesters. Observations are expected to be completed in mid-2008. The target sample consists of about 30 Lyman Break Galaxies (LBGs), most of which at $3<z<3.7$, and only a few of them at $4.3<z<5.2$. A more detailed discussion on the sample selection is given in section 2.1. In this paper we present preliminary results based on a first set of data for 9 galaxies, and restricted to the redshift range $3<z<3.7$ (Tab. 1). The integration times range from 3 to 7.5 hours on source. The goal of the SINFONI observations is to determine the gas metallicities by means of a combination of strong line diagnostics based on $H\beta$ and [OIII]5007 shifted into the K band, as well as [OII]3727 and [NeIII]3870 shifted into the H band for sources at $3<z<3.7$. At $4.3<z<5.2$ we only rely on the [OII]/[NeIII] ratio observed in the K band (but sources in this redshift interval will not be discussed here). Details on the gas metallicity determination are given in section 5.

The two-dimensional spectroscopic capabilities of SINFONI are obviously exploited also to map the emission lines. However, the two-dimensional analysis of the spectra goes beyond the scope of this paper and will be discussed in a separate paper.

2.1. Sample selection

Galaxies in our sample are selected among $z>3$ galaxies primarily identified through the Lyman-break technique, mostly from the Steidel et al. (2003) survey and from the deep spectroscopic surveys in the Chandra Deep Field South (CDFS) (e.g. Vanzella et al., 2006), but we also included some lensed galaxies (e.g. Frye et al., 2002, 2007) to better explore the low mass end (but none of the lensed galaxies is in the preliminary sample presented in this paper). Galaxies were selected only amongst those with highly reliable spectroscopic redshift (e.g. flagged as ‘‘A’’ in Vanzella et al., 2006). We required that the redshift is such that the emission lines of interest for the metallicity determination ([OIII], $H\beta$, [OII], [NeIII]) are out of strong sky emission lines and out of deep atmospheric absorption features. Actually, these requirement could not always be fulfilled for all of the emission lines (also because sometimes the redshift determined through optical spectra is not accurate, due to winds affecting UV-rest frame features, or IGM absorption of the Ly α); however, in these cases any contamination by OH lines or lower S/N due to atmospheric absorption will be fully taken into account when estimating the metallicity.

The additional requirement is that the source has been observed with at least two of the Spitzer-IRAC bands, which at these redshifts sample the rest-frame near-IR light. IRAC data are required for a reliable determination of the stellar mass (see §6). Finally, we excluded sources whose optical spectrum shows indications for the presence of an AGN. Moreover, for most of the sources we also required that deep hard X-ray data and mid-IR Spitzer-MIPS data are available, to better exclude the presence of a hidden AGN, as discussed in §2.2.

In this paper we only present results for an initial sub-sample of nine sources at $3<z<3.7$, for which data have been already obtained and reduced. The list of sources, along with some of their photometric properties, is given in Tab. 1. Tab. 2 lists some

of the physical properties of these sources as inferred from their broad-band spectral energy distribution. A detailed discussion on the extraction of these parameters will be given in §6.

2.2. AGNs removal

The presence of an AGN, contributing to the gas ionization, affects the observed emission line ratios. In this case the metallicity diagnostic diagrams calibrated on star forming galaxies are not usable, since the excitation mechanism is totally different. As a consequence, galaxies hosting AGNs must be carefully avoided.

A first step is to exclude galaxies whose optical spectrum (UV rest frame) shows indications for the presence of an AGN (e.g. NV, CIV, HeII, or broad Ly α). However, the absence of optical-UV AGN-like lines is a required condition, but not sufficient to rule out the presence of an AGN. Indeed, even if an AGN is present, the associated optical-UV emission lines may be undetected either because obscured by dust (either on small scales, for the BLR, or on larger scales, for the NLR), or because their Narrow Line Region is not developed (e.g. Maiolino et al., 2003; Martínez-Sansigre et al., 2006).

An additional constraint comes from hard X-ray data. In many of the fields used by us, deep Chandra observations allow the detection of obscured (Compton thin) AGNs up to $z \sim 4$, even at Seyfert-like luminosities. Therefore, an additional requirement was that our sources are not detected in the hard X-rays (2–8 keV). They should not be detected also in the soft X-rays (0.5–2 keV) at a level higher than expected by strongly star forming galaxies (actually none of the galaxies is detected even in the soft band). In the CDFS the deep X-ray data allow us to exclude the presence of obscured, Compton thin AGNs with 2–10 keV luminosity higher than about 5×10^{43} erg s $^{-1}$ (i.e. in the Seyfert range).

However, current X-ray surveys are not deep enough to detect Compton thick AGNs, whose emission is strongly suppressed even in the hard X-rays. This issue was made clear by recent Spitzer results (Martínez-Sansigre et al., 2007; Alonso-Herrero et al., 2006; Polletta et al., 2006; Fiore et al., 2007; Daddi et al., 2007). Indeed, Spitzer observations have revealed the presence of obscured AGNs, through the associated mid-IR hot dust emission, even in high- z galaxies that are undetected in deep hard X-ray observations. These are shown to be high- z Compton thick (or nearly Compton thick) AGNs, which remained elusive to previous optical and X-ray surveys. Deep 24 μ m Spitzer-MIPS data were found to be particularly efficient to identify high- z obscured AGNs, even at relatively low intrinsic luminosities. As a consequence, we requested that our sources have deep MIPS data at 24 μ m. Fiore et al. (2007) showed that the mid-IR excess relative to the optical emission ($F_{24\mu\text{m}}/F_R$), is a good tracer of obscured AGNs at high redshift. As listed in Tab 1, most of our sources are undetected at 24 μ m. More specifically, all our sources have a ratio $F_{24\mu\text{m}}/F_R < 10$, which is significantly lower than expected for Sy2s and QSO2s at $z \sim 3$ ($F_{24\mu\text{m}}/F_R \sim 20 - 3 \cdot 10^4$), therefore ruling out the presence of AGNs (both Compton thick and thin) even at Seyfert-like luminosities.

3. Observations and data reduction

The near-IR spectroscopic observations were obtained by means of SINFONI, the integral field spectrometer at VLT. SINFONI was used in its seeing-limited mode, with the 0.25'' pixel scale

and with the H+K grism, yielding a spectral resolution $R \sim 1500$ over the spectral range 1.45–2.41 μ m.

Each target was acquired through a blind offset from a nearby bright star. Each observing block consisted of 10 integrations, 5 minutes each, obtained by nodding the position of the source within the 8'' \times 8'' SINFONI field of view (generally by locating the source in two opposite corners). This observational procedure allows background subtraction by using frames contiguous in time, but with the source in different locations. Moreover, the source was never located at the same position in the FOV: a minimal dithering of 0.5'' was required, so that instrumental artifacts can be minimized when the individual observations are aligned and combined together. The (K-band) seeing during the observations was generally better than 0.8''. Each source was observed with a number of observing blocks ranging from 5 to 9. Some observing block was discarded because the seeing was much worse, or the background much higher, with respect to the other observing blocks. The total on-source integration times are listed in Tab. 1.

Data were reduced by using the ESO-SINFONI pipeline (version 3.6.1). The pipeline subtracts the sky from the temporally contiguous frames, flat-fields the images, spectrally calibrates each individual slice and then reconstructs the cube. Residual sky emission was accounted for by removing the median of each spectral plane; this is feasible because our source occupy only a small part of the field of view. In some cases we performed an additional step in the background subtraction (which resulted imperfect with the previous method probably because of minor uncertainties in the flat-fielding) by sampling the sky in a region outside the source (either annular or another region in the field of view observed with the same effective integration) and rescaling it to optimally subtract the sky lines on the spectrum of the source. Individual cubes were aligned in the spatial direction by relying on the telescope offsets and then averaging them together by applying a 2σ clipping to remove bad pixels and cosmic rays.

The atmospheric absorption and instrumental response were corrected by dividing the spectrum of the scientific target by the spectrum of a star (spectral type OV-BV or GV) taken close to the source, both in time and in elevation. The intrinsic spectrum of the star was removed by dividing the observed stellar spectrum by the appropriate template given in Pickles (1998), or by the solar spectrum in the case of GV stars (Maiolino et al., 1996).

4. Results and data analysis

We extracted the spectra within a fixed aperture of 0.75'' in diameter (corresponding to ~ 6 kpc projected on sources at $z \sim 3.5$), which in most cases encloses more than 70% of the emission line flux and generally maximizes the S/N ratio. However, one should keep in mind that there are metallicity gradients within each galaxy and therefore the aperture choice may introduce biases, especially for what concerns the comparison with low redshift surveys. This issue will be discussed more extensively in §7.2. An exception is SSA22a-aug96M36, whose line emission extends significantly beyond the 0.75'' aperture; in this case we adopted an aperture of 1.25''. The resulting spectra, smoothed with a 2 pixel boxcar to improve the signal-to-noise, are shown in Figs. 1–3. The location of [OII]3727, [NeIII]3870 (when observable), H β , [OIII]4959 and [OIII]5007 is indicated with vertical dashed lines. In each spectrum the bottom panels show the sky spectrum. The shaded vertical regions overlaid on each spectrum highlight spectral regions affected by strong sky emission

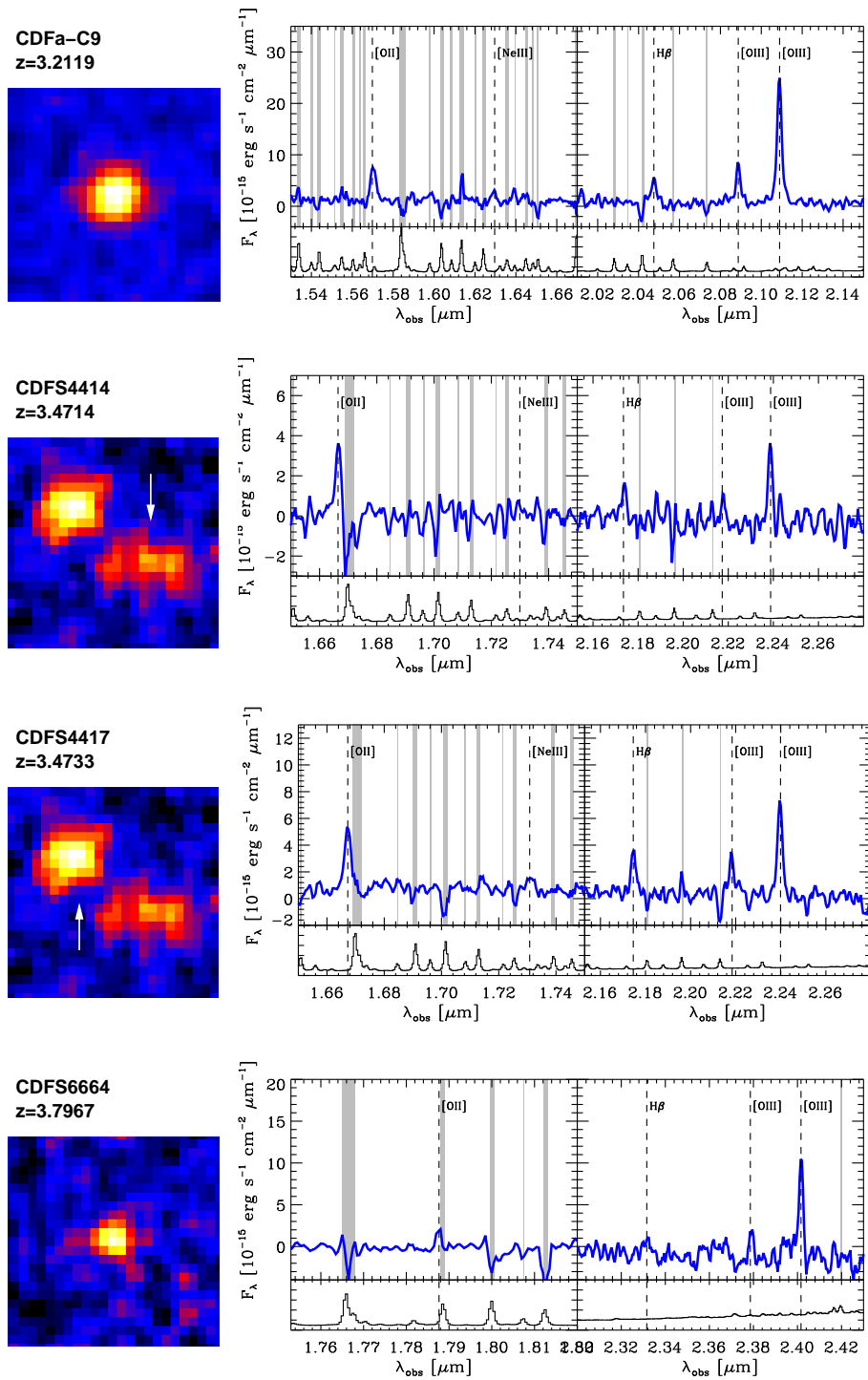


Fig. 1. [OIII]5007 line maps (left) and near-IR spectra (right) of the galaxies in the AMAZE sample presented here. Each [OIII]5007 map has a size of $3'' \times 3''$. The vertical dotted lines in the spectra indicate the expected location of nebular emission lines. The bottom panels show the sky spectrum. The shaded vertical regions overlaid on each spectrum highlight spectral region affected by strong emission lines.

lines. In Figs. 1-3 we also show the [OIII]5007 line map of each source.

Fig. 4 shows the composite spectrum of all nine sources, obtained by shifting the spectra to the rest-frame, resampling them to a common wavelength scale, normalizing them by the flux of H β and averaging them. We excluded spectral regions strongly affected by atmospheric absorption within individual spectra.

The stellar continuum is detected only in a few cases, and even in these cases the continuum is only seen in the map produced by stacking the cube in the spectral direction in the K or H band.

The emission line fluxes were measured by fitting a single gaussian over a linearly interpolated, underlying continuum (which may be some weak stellar continuum or, more often, residual thermal background or residual bias subtraction). The

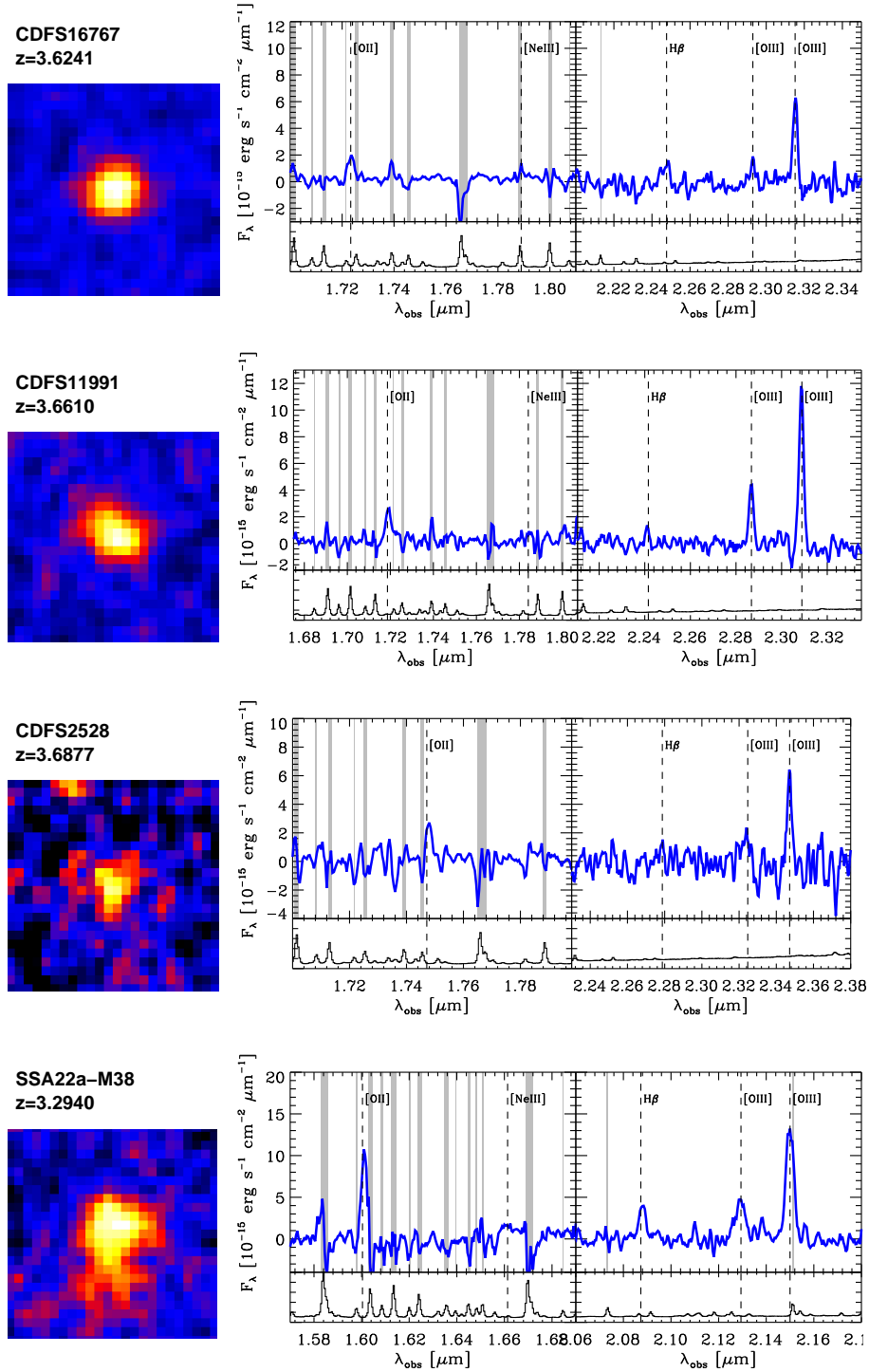


Fig. 2. Same as Fig. 1 for four additional sources.

resulting line fluxes are given in Tab. 3. Note that for what $H\beta$ is concerned we do not perform any subtraction of a stellar component, since the stellar continuum is always very weak and generally undetected, hence the correction for any putative stellar $H\beta$ is negligible. Some authors apply a fixed correction of 2\AA for the EW of a putative $H\beta$ in absorption; in our case such a correction would generally affect the inferred metallicities by less than 0.03 dex.

5. The gas metallicity

5.1. Metallicity diagnostics and calibrations

The only method to determine the gas metallicity in faint distant emission line galaxies is to use strong line metallicity diagnostics. Essentially, the ratio between various strong, optical emission lines is found to depend on the gas metallicity, either directly and/or through other dependences (e.g. the metallicity dependence of the ionization parameter, gas density, hardness of ionizing radiation, etc...). Various strong line ratios have been calibrated against metallicity, either determined “directly”

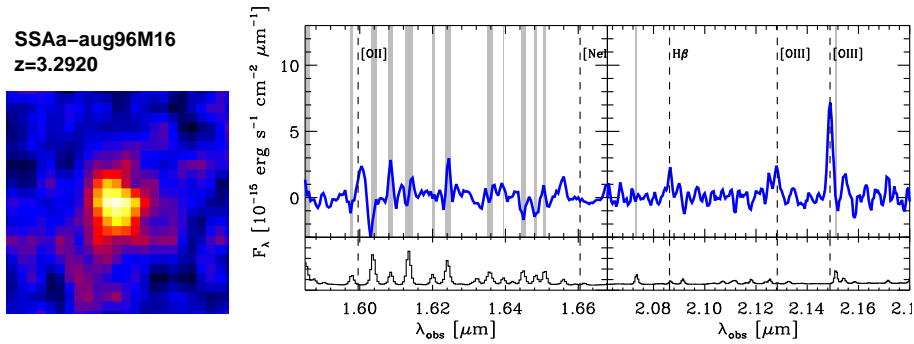


Fig. 3. Same as Figs. 1-2 for one additional source.

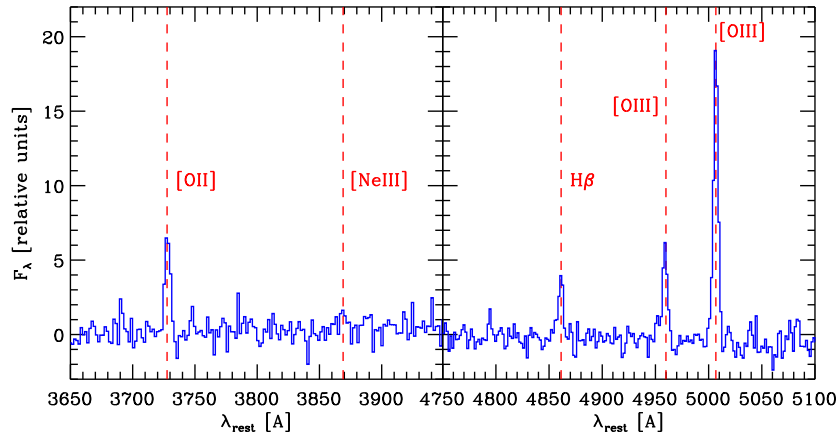


Fig. 4. Composite spectrum of the nine sources presented in this paper.

(e.g. through the electron temperature T_e method) or “indirectly” (e.g. through photoionization models). However, such calibrations have often been performed in relatively narrow metallicity intervals, not adequate to explore the wide metallicity range spanned by galaxies through the cosmic epochs, as we shall see. Another serious problem is that such calibrations are often inconsistent with each other: the same galaxy is found to have significantly different metallicities if different strong-line diagnostics are adopted. This issue has been reviewed in detail by Kewley & Ellison (2008). Obviously, a wrong intercalibration between different metallicity diagnostics has dramatic implications for the investigation of the metallicity evolution. Indeed, at different redshifts people have observed different emission lines, depending on the adopted band, and therefore an incorrect intercalibration between the various diagnostics may hamper the capability of investigating evolutionary effects, or may even introduce artificial trends.

To minimize this issue it is recommended to use the same strong line calibration method for all objects at various redshifts and from different surveys, or to convert the strong line calibrations adopted by different authors to a common calibration scale (e.g. by using the conversion formulas given in Kewley & Ellison, 2008). However, the problem that we face in this paper is that no single strong line calibration method exists over the wide metallicity range spanned by galaxies through the cosmic epochs (as we shall see). Some methods nominally span a somewhat wider metallicity range, but they are known to run into serious troubles in some metallicity intervals.

The electron temperature T_e method (e.g. by exploiting the intensity of the [OIII]4636 auroral line) provides a good measure of the metallicity below about $12+\log(\text{O}/\text{H})<8.3$ (e.g.

Pilyugin, 2001; Pettini & Pagel, 2004), and can be used to calibrate the strong line ratios in this range. The reliability of the T_e method in the low metallicity range is confirmed by the comparison with the stellar (OB) photospheric metallicity measurements (Bresolin et al., 2006b, 2007b). The T_e method has been extended to higher metallicities by various authors (Kennicutt et al., 2003; Garnett et al., 2004; Liang et al., 2007; Yin et al., 2007). However, at high metallicities the T_e method tends to saturate and to underestimate significantly the true metallicity, due to temperature fluctuations and gradients, both within individual HII regions and over the whole galaxy. This issue is expected theoretically (Stasińska, 2005) and verified observationally by the comparison with the metallicities determined through recombination lines, which are insensitive to temperature fluctuations (Bresolin, 2006a, 2007a).

Photoionization models are an alternative way of calibrating strong line ratios (e.g. Tremonti et al., 2004; Kewley & Dopita, 2002; Zaritsky et al., 1994), especially at high metallicities, where most of these studies apply. However, all photoionization models are subject to significant uncertainties and possible systematic effects. The observed spread in calibration between different models highlights this problem (Kewley & Ellison, 2008). The photoionization models presented in Kewley & Dopita (2002) are probably not free from the uncertainties and possible systematic effects discussed above, however they provide results which are intermediate among other photoionization models (Kewley & Ellison, 2008), and therefore can be considered fairly representative of this class of calibrations. Moreover, independent “direct” determinations of the metallicity (by exploiting the temperature-insensitive method of recombination lines, Bresolin, 2006a, 2007a) are in fair agreement with the photoion-

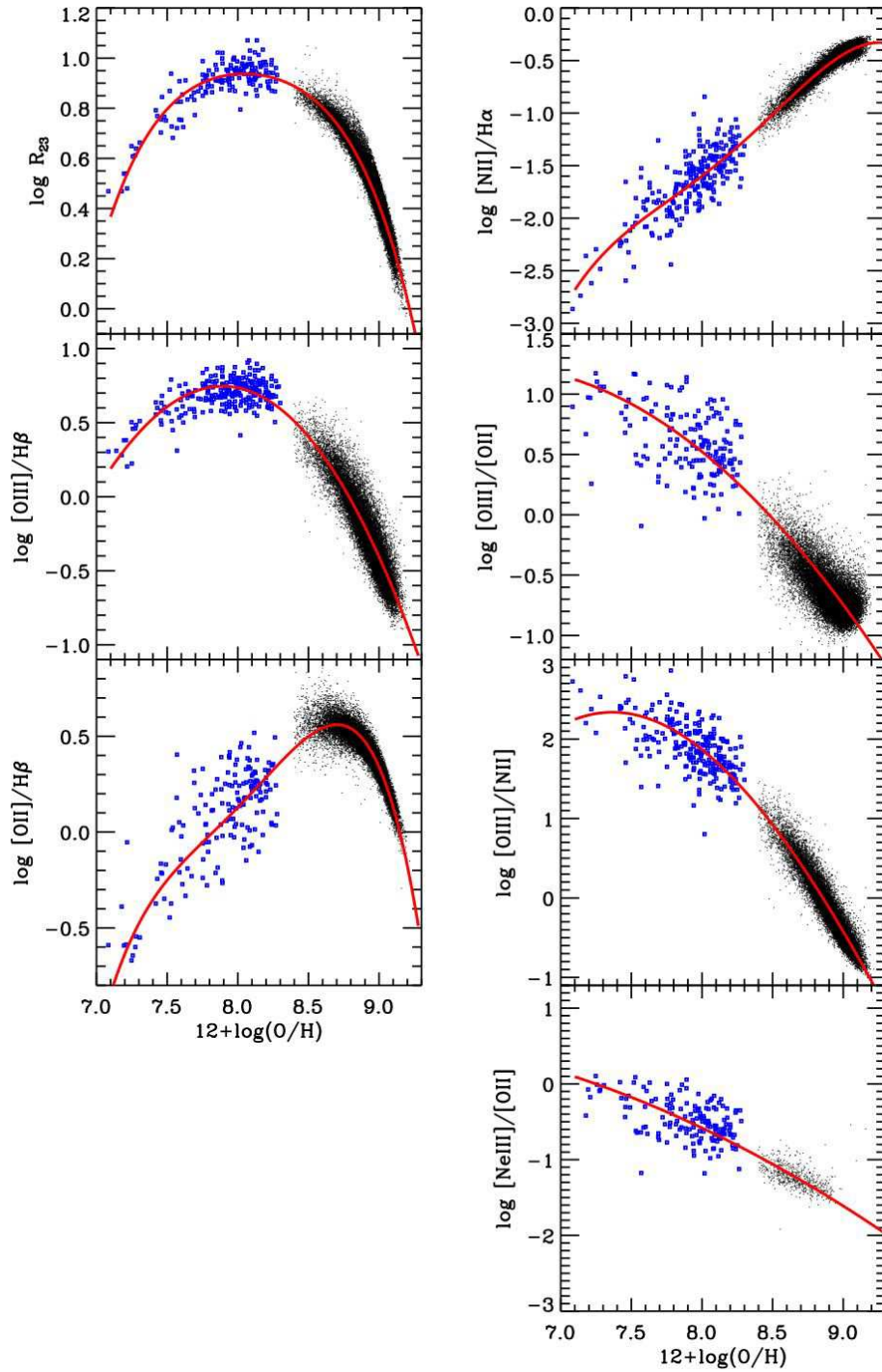


Fig. 5. Relations between strong emission line ratios and gas metallicity. Blue squares are low metallicity galaxies (from Nagao et al., 2006) for which the metallicity is inferred through the electron temperature T_e method. Black dots are SDSS DR4 galaxies for which metallicities are inferred through the photoionization models in Kewley & Dopita (2002). The red line curve shows a polynomial fit to the relations in the form given by Eq. 1 with the coefficients given in Tab. 8

ization models provided by Kewley & Dopita (2002). The latter did not investigate photoionization models at metallicities $12 + \log(\text{O}/\text{H}) < 8.4$. Other studies attempt to extend photoionization models to $12 + \log(\text{O}/\text{H}) < 8.3$, but fail to reproduce the observed line ratios (e.g. Dopita et al., 2006).

Since no single method is capable of providing a calibration of the strong line diagnostics over the wide metallicity range required to sample the evolution of galaxies through the cosmic

epochs ($7.7 < 12 + \log(\text{O}/\text{H}) < 9.1$), in this paper we have to combine two different methods depending on the metallicity range.

At low metallicities ($12 + \log(\text{O}/\text{H}) < 8.35$) we use calibrations of the strong-line diagnostics based on the T_e method, which is regarded as reliable at low metallicities and free of problems related to temperature fluctuations and gradients (Stasińska, 2005; Bresolin et al., 2006b, 2007b). We use the sample of 259 low metallicities galaxies gathered by Nagao et al. (2006) for which measurement of the auroral line $[\text{OIII}]\lambda 4636$ is

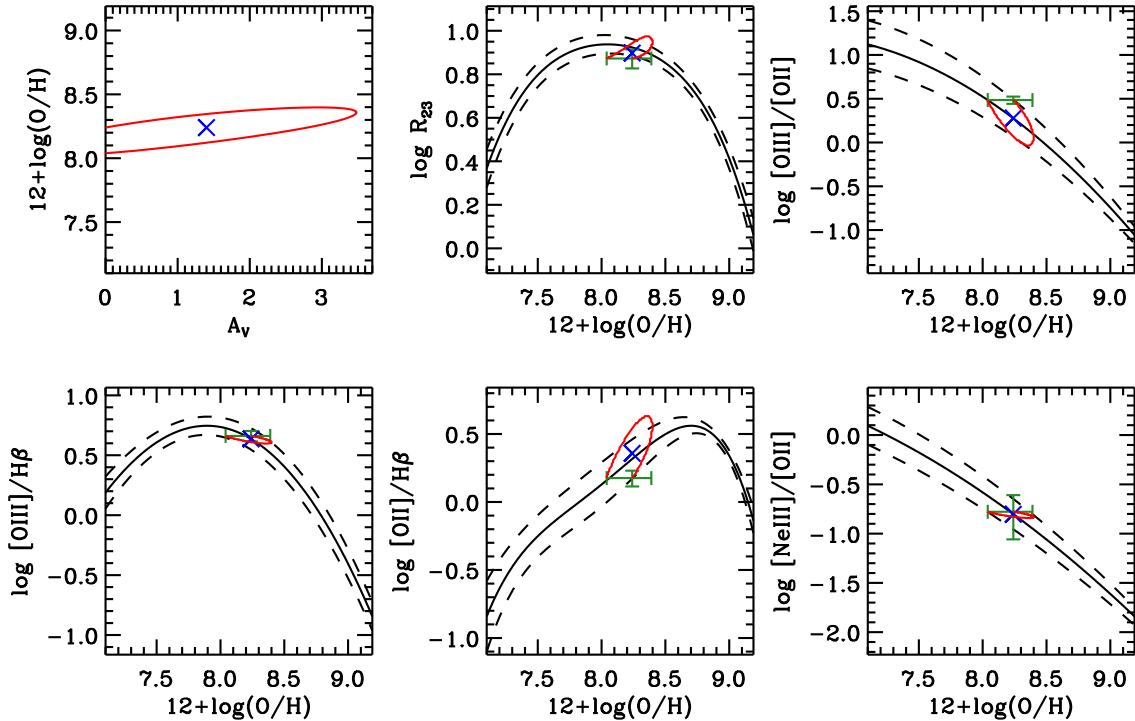


Fig. 6. Example of the diagnostic tools used to determine the metallicity in the specific case of the composite spectrum. The upper left panel shows the best solution (blue cross) and the 1σ confidence level in the A_V –metallicity plane. In the other panels the black solid line (best fit) and the dashed lines (dispersion) show the empirical relations between various line ratios and the gas metallicity (see Fig. 5). The green errorbars show the observed ratios (along the Y-axis) and the best-fit metallicity with uncertainty (along the X-axis); the blue cross shows the de-reddened ratios, by adopting the best-fit extinction; the red line shows the projection of the 1σ uncertainty of the fit in the top-left panel.

available. The metallicity determination based on the T_e method is detailed in Nagao et al. (2006). The inferred metallicities for this sample are in the range $7.1 < 12 + \log(O/H) < 8.3$. The inferred empirical relations between metallicity and various strong-line diagnostics are shown in Fig. 5 with blue squares. Note that the T_e method is only used to calibrate the strong line diagnostics in local galaxies (and at low metallicities), but it will not be used to directly measure metallicities in our high- z objects, since the [OIII]4636 line is too faint to be detected.

At $12 + \log(O/H) > 8.35$, where the T_e method is known to fail (as discussed above), we have to rely on photoionization models. More specifically, we adopt the calibrations provided by the models in Kewley & Dopita (2002), aware of the caveats discussed above, and in particular that these models are valid only at $12 + \log(O/H) > 8.4$. We then used the data of star forming galaxies in SDSS DR4, by adopting the same constraints on the signal-to-noise discussed in Nagao et al. (2006), and by also considering only objects with $\log([\text{NII}]6564/[\text{OII}]3727) > 1.2$, as recommended by Kewley & Dopita (2002). This selection results in a total of 22,482 objects. After determining the gas metallicity for each object with the Kewley & Dopita (2002) method, we derived the empirical relations with various strong-line diagnostics as shown in Fig. 5 (black dots).

The relations obtained by combining both the low metallicity and the high metallicity samples were fitted with a polynomial curve. To avoid the fit to be dominated by the regions containing the largest number of objects (i.e. by the SDSS sample at $8.7 < 12 + \log(O/H) < 9.1$), we divided the relations in metallicity bins (generally spaced by 0.1 dex), we derived the median and dispersion of the strong-line flux ratio and of the stellar masses within each bin, and then fitted the polynomial function

to these medians. In most cases a second order or a third order polynomial is appropriate to describe the relation over the full metallicity interval. However, in some cases a fourth order polynomial is required. The general functional form for describing the strong-line metallicity calibration is therefore:

$$\log R = c_0 + c_1x + c_2x^2 + c_3x^3 + c_4x^4 \quad (1)$$

where $\log R$ is the logarithm of the strong-line ratio, and x is the metallicity relative to solar ($x = \log(Z/Z_\odot) = 12 + \log(O/H) - 8.69$, Allende Prieto et al. (2001)). The coefficients $c_0 - c_4$ for each strong-line ratio are listed in Tab. 8, and the resulting best fit polynomials are plotted with a solid red curve in Fig. 5.

5.2. Determination of the gas metallicity

In the redshift range $3 < z < 3.7$ investigated in this paper [OII]3727 and (not always) [NeIII]3870 are observable in the H band, while $H\beta$ and [OIII]5007 are observable in the K band. This allows us to use five metallicity diagnostics (not all of them independent of each other), namely: $R_{23} = ([\text{OII}]3727 + [\text{OIII}]4959 + [\text{OIII}]5007)/H\beta$, $[\text{OIII}]5007/H\beta$, $[\text{OII}]3727/H\beta$, $[\text{OIII}]5007/[\text{OII}]3727$, $[\text{NeIII}]3870/[\text{OII}]3727$. The relationship between these ratios and the gas metallicity, along with their dispersion, are shown in Figs. 5 and 6. Each of these diagnostics has advantages and disadvantages. For instance, $[\text{OIII}]5007/H\beta$ is essentially unaffected by dust reddening, but it has a double metallicity solution for each value of this ratio. $[\text{OIII}]5007/[\text{OII}]3727$ has a monotonic dependence on metallicity, but it is potentially affected by dust reddening and it is also affected by a larger dispersion. $[\text{NeIII}]3870/[\text{OII}]3727$ is

both a monotonic function of metallicity and little affected by dust reddening, nonetheless [NeIII] is generally the faintest of all these lines and the most difficult to detect. However, if these various diagnostics are used simultaneously, then it is possible to both account for dust reddening and remove the ambiguity of double solutions. Essentially, if all the diagnostics are used then only some combinations of metallicity and dust reddening are allowed by the data.

More specifically, we selected the following independent metallicity diagnostics: [OIII]5007/H β , [OIII]5007/[OII]3727 and (when available) [NeIII]3870/[OII]3727 (note that the ratio [OIII]5007/H β is very similar to the “classical” R_{23} parameter at the low metallicities investigated by us, since at low metallicities [OIII]/[OII] is high). We then determined the best pair of metallicity and extinction that minimizes the χ^2 in the three corresponding diagrams, both by including the measurement errors and the dispersion of each calibration diagram. In practice, since [NeIII] is often undetected or not observable, the metallicity is mostly determined through the [OIII]5007/H β ratio, while the [OIII]5007/[OII]3727 ratio is used to discriminate which of the two metallicity solutions for the [OIII]5007/H β ratio applies and also to provide some constraints on the dust extinction (although the latter has generally negligible effect on the metallicity determination since [OIII]5007/H β is insensitive to reddening).¹

As an example, we show the results of this method in Fig. 6 in the case of the composite spectrum. The upper left panel shows the best solution (blue cross) and the 1σ confidence level (red curve, obtained from solutions with $\Delta\chi^2 = 1$) in the A_V –metallicity plane. In the other panels the black solid line (best fit) and the dashed lines (dispersion) show the empirical relations between various line ratios and the gas metallicity (Fig. 5); the green errorbars show the observed ratios (along the Y-axis) and the best-fit metallicity with uncertainty (along the X-axis); the blue cross shows the de-reddened ratios, by adopting the best-fit extinction; the red line shows the projection of the 1σ uncertainty of the fit obtained in the top-left panel. It can be noted that the extinction is subject to a large uncertainty, but the metallicity is relatively well constrained. The metallicities resulting from the procedure discussed above are listed for all objects and for the composite spectrum in Tab. 3.

5.3. Evolution of the metallicity diagnostics

One of the main worries when using strong emission line diagnostics in high- z sources is that the empirical calibrations are obtained by using local sources. Since the dependence of the strong lines ratios on metallicity involves also other dependences (e.g. on the ionization parameter, on the shape of the ionizing radiation, on the gas density), the evolution of the average galaxy properties (e.g. SFR, compactness) with redshift may affect the calibration of the metallicity diagnostics. It is very difficult to investigate this issue, since in principle one would need to obtain an empirical calibration at high- z by observing primary metallicity tracers (e.g. [OIII]4636), which are however extremely faint. An alternative way is to construct diagrams which are sensitive to the excitation mechanism, by disentangling the dependence on metallicity, and verify whether the line excitation conditions change with redshift.

Such a test was performed, at lower redshifts, by investigating the diagram [OIII]/H β versus [NII]/H α for sources where

¹ For the A_V –metallicity fit we used the Milky Way extinction curve (Cardelli et al., 1989) ($R_V = 3.1$), which is often preferred for the nebular lines.

all of these lines are observable (Shapley et al., 2005; Erb et al., 2006; Liu et al., 2008). It is found that a fraction of sources at $z \sim 1-2$ are offset with respect to the sequence described by local HII galaxies, and displaced towards the AGN locus. An interpretation is that at least some of these sources are affected by some AGN contribution (Liu et al., 2008), which were not excluded from the sample because elusive in the UV rest-frame spectra. Other sources may be characterized by truly different physical conditions with respect to local HII regions, and in particular higher ionization parameter. However, even in the latter cases both Brinchmann et al. (2008) and Liu et al. (2008) find that the calibration of the strong line metallicity diagnostics do not deviate by a large amount with respect to local HII galaxies. In particular, they find deviations by only about 0.1 dex (or less) in terms of metallicity calibration, depending on the specific diagnostic adopted.

For what concerns the sources at $z \sim 3.5$ in AMAZE, the available emission lines allow us to construct the so-called BPT diagram (Baldwin et al., 1981), i.e. [OIII]5007/H β versus [OIII]5007/[OII]3727. As discussed in Dopita et al. (2006) this diagram is strongly degenerate in terms of metallicity, but it is sensitive to both the ionization parameter and the hardness of the ionizing source. Within the observational uncertainties, the sources in our AMAZE sample do not deviate from the sequence of local HII galaxies on the BPT diagram, suggesting that the excitation conditions do not differ significantly from the local galaxies used to calibrate the strong metallicity diagnostics.

6. Stellar masses

To derive the stellar masses for the LBGs in the AMAZE sample, we used an approach based on broad-band spectral fitting technique. Broad-band photometric data for the sources in the CDFS were collected from the GOODS–MUSIC multiwavelength catalog (Grazian et al., 2006). This catalog provides photometric data in 14 spectral bands (from UV to the Spitzer-IRAC bands), and it has been recently updated to include the Spitzer–MIPS data at $24\mu\text{m}$. For the LBGs in Steidel et al. (2003), optical photometric data (U,G,R,I) were extracted from the publicly available images (Steidel et al., 2003), while Spitzer IRAC and MIPS data were obtained from the Spitzer archive; the photometry extraction was performed following the same methods described in Grazian et al. (2006).

The SED fitting technique adopted here is the same as in previous papers (Fontana et al., 2006; Grazian et al., 2006, 2007), and similar to those adopted by other groups in the literature (e.g. Dickinson et al., 2003; Drory et al., 2004; Pozzetti et al., 2007). This technique is based on comparing the observed multicolor distribution of each object and a set of templates, computed with standard spectral synthesis models (see below) and chosen to broadly encompass the variety of star–formation histories, ages, metallicities, and extinction of real galaxies. More specifically, we considered exponentially decaying SFR with e-folding times ranging from 0.1 to 15 Gyr. We used the Salpeter IMF ($M_{min} = 0.1M_\odot$ and $M_{max} = 65M_\odot$), ranging over a set of metallicities (from $Z = 0.02Z_\odot$ to $Z = 2.5Z_\odot$) and dust extinction ($0 < E(B - V) < 1.1$, with a Calzetti et al. (2000) attenuation curve, which is generally more appropriate for the stellar component). For each model of this grid, we computed the expected magnitudes in our filters set and found the best-fitting template with a standard χ^2 normalization. The stellar mass and other best-fit parameters of the galaxy, like SFR, age, and dust extinction, are fitted simultaneously to the actual SED of the observed galaxy. The metallicity of each galaxy is fixed to value

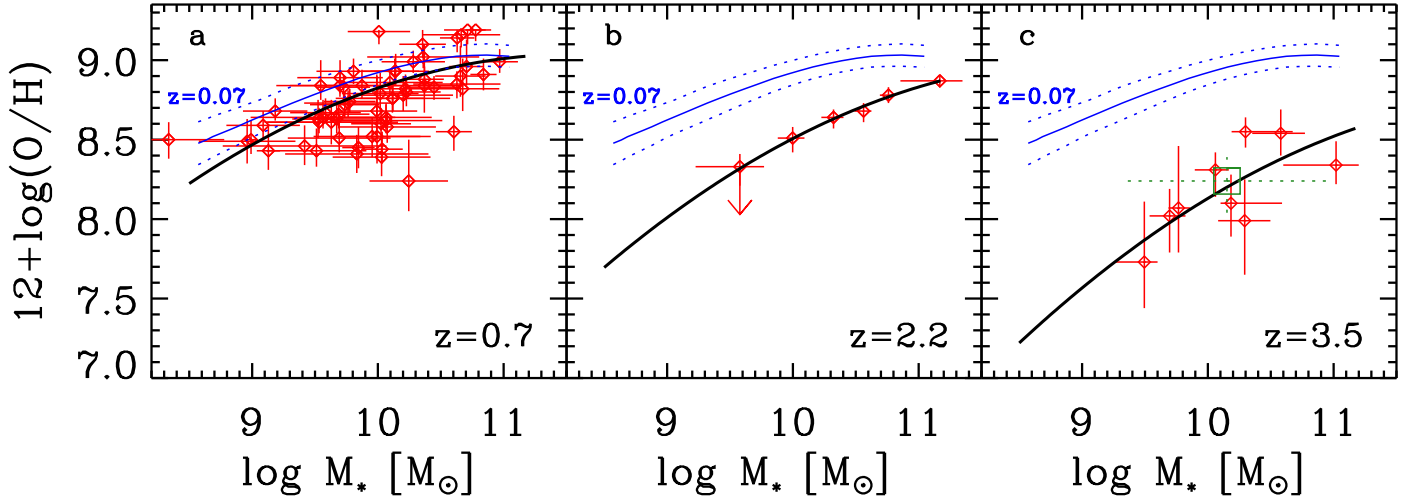


Fig. 7. Mass-metallicity relation observed at different redshifts. The blue, solid and dotted lines indicate the mass-metallicity relation and its dispersion observed at $z\sim 0.07$, as inferred by Kewley & Ellison (2008). The red diamonds with errorbars show the mass-metallicity relation at different redshifts traced by individual objects (or by stacked spectra in the case of panel *b*, $z\sim 2.2$). In panel *c* ($z\sim 3.5$) the green square with dashed errorbars is the composite spectrum (which has been assigned the median mass of the sample, but slightly offset to avoid a confusing overlap with an individual source). Black, solid lines show the analytical function Eq. 2 with the best fitting parameters listed in Tab. 5.

closest to the one determined by us through the nebular lines (Tab. 3).

The stellar mass derived here is subject to uncertainties and biases related to the synthetic libraries used to carry out the fitting of the galaxy SEDs. In general, the stellar mass turns out to be the least sensitive parameter to variations of the input model assumptions, and the extension of the SEDs to mid-IR wavelengths (near-IR rest-frame) with IRAC greatly reduces the formal uncertainties on the derived stellar masses, as shown in Fontana et al. (2006). The uncertainties in the stellar mass are derived as follows: we compute the 90% confidence level on the mass by scanning the χ^2 levels, fixing the redshift and the metallicity for each galaxy but allowing the other parameters (SFR, age, dust extinction) to change.

Age and star formation rate are more uncertain parameters to derive. In some cases we formally obtain best-fit ages below ~ 50 Myr, which are below the dynamical timescales for the star forming regions in these systems (Shapley et al., 2001). Moreover, the conversion between UV luminosity and SFR becomes highly non-linear below this age. As a consequence, we decided to restrict the allowed ages to >50 Myr. However, this choice may only affect the inferred SFR, while the determination of the stellar mass is essentially unaffected, as discussed above.

For what concerns the library of spectral synthesis models we adopt both those provided by Bruzual & Charlot (2003) (hereafter BC03) and those by Maraston (2005) (hereafter M05). The resulting stellar masses are tabulated for both cases in Tab. 2. The masses inferred by using the M05 models are preferred, since they take into account the contribution by TP-AGB stars, and may differ from the stellar masses obtained with BC03 by even a factor of two, especially in older stellar systems. However, previous works on the mass-metallicity relation at lower redshift adopted the BC03 templates. Therefore, when comparing our results with the previous works at lower redshifts we will adopt for consistency the masses obtained with the BC03 templates. In Tab. 2 we also list the SFR, age and reddening inferred by the SED fitting (adopting templates by BC03, again for a consistent comparison with previous works).

7. The mass–metallicity relation at high redshift

7.1. Comparing the mass-metallicity relation at different redshifts

Different studies of the mass-metallicity relation at various redshifts have employed different diagnostic lines and different calibrations. As discussed in §5 and more extensively in Kewley & Ellison (2008), the mismatch between the different calibration scales may introduce artificial evolutionary effects of the mass-metallicity relation. Therefore, it is important that different strong-line diagnostics used in different surveys are cross-calibrated in a consistent way. The relations obtained in §5 provide such a common cross-calibration between different strong-line diagnostics on the same metallicity scale. In this section we apply (when required) the correction to the metallicities inferred by past surveys at lower redshift to match our metallicity scale. We also apply corrections to the mass scale to account for the different IMF’s adopted by previous works.

As discussed in §1 the local ($z\sim 0.1$) mass-metallicity relation was derived by Tremonti et al. (2004) by using SDSS spectra from DR2. Kewley & Ellison (2008) re-determined the local mass-metallicity relation by using SDSS spectra from DR4 by setting tighter limits on the redshift range ($0.04 < z < 0.1$) so that the projected SDSS fiber covering factor is $>20\%$ of the total photometric g' -band light, and also to minimize incompleteness effects at higher redshifts. The resulting median redshift of their sample is ~ 0.07 . Kewley & Ellison (2008) calibrate the metallicities with the Kewley & Dopita (2002) method, which is the same adopted by us at $12 + \log(O/H) > 8.35$, hence no additional correction is required to match our metallicity scale. The only correction to apply is for the stellar masses, since Tremonti et al. (2004) and Kewley & Ellison (2008) adopt a different IMF (Kroupa, 2001). We calculate that the masses in Kewley & Ellison (2008) must be multiplied by a factor of 1.17 to comply with our IMF (note that the IMF’s differs not only in terms of shape but also in terms integration limits). The thin blue solid lines in Fig. 7 show the Kewley & Ellison (2008)

mass-metallicity relation corrected as discussed above. The blue, dotted lines indicates the 1σ dispersion of the same relation.

At $0.4 < z < 1$ we use the results by Savaglio et al. (2005). For consistency with our calibration scale we re-determine the metallicities for each object in their sample by applying the same procedure described in §5.2 to the line fluxes tabulated by them. We exclude from their sample objects without K-band data, since in these cases the stellar mass uncertainties are too large. We also have corrected the stellar masses in Savaglio et al. (2005) by a factor of 1.4 to comply with the IMF adopted by us. The resulting mass-metallicity relation at $z \sim 0.7$ is shown with red diamonds and errorbars in Fig. 7a.

At $z \sim 2.2$ we use the results by Erb et al. (2006), who infer the metallicity of LBG’s at this redshift through the [NII]/H α ratio measured in *stacked* spectra. Also in this case we re-determine the metallicity in each mass bin by using the [NII]/H α metallicity calibration obtained in §5, to be consistent with the calibrations adopted by us. The stellar masses in Erb et al. (2006) have to be corrected by a factor of 1.4 to comply with the IMF adopted by us. The resulting mass metallicity relation at $z \sim 2.2$ is shown with red diamonds and errorbars in Fig. 7b.

Finally, Fig. 7c shows the mass-metallicity relation inferred from the initial sample of nine AMAZE sources at $z \sim 3.5$. The red diamonds with solid errorbars are individual objects. The green square with dashed errorbars is the composite spectrum. In this plot, for consistency with the other works at lower redshifts, we use the stellar masses inferred with the BC03 templates.

Previous versions of our mass-metallicity relation $z \sim 3$, presented in our previous preliminary works (Maiolino et al., 2007a,b), were slightly different because of lower S/N spectra and also because we used different calibrations (both for metallicity and stellar masses).

For a more straightforward comparison of the mass-metallicity relation at different redshifts, it is useful to describe these relations by fitting them with the same functional form. In order to minimize the number of free parameters we find statistically satisfactory an approach similar to Savaglio et al. (2005): the quadratic function fitting the local mass-metallicity relation is shifted in mass and in metallicity to provide the best fit of the mass-metallicity relation at various redshifts. More specifically we adopt the following description of the mass-metallicity relation:

$$12 + \log(\text{O}/\text{H}) = -0.0864 (\log M_* - \log M_0)^2 + K_0 \quad (2)$$

where $\log M_0$ and K_0 are determined at each redshift to obtain the best fit to the observed data points², as listed in Tab. 5.

7.2. Aperture effects

Since galaxies, and especially disk galaxies, are often characterized by metallicity gradients (the metallicity decreasing towards the outer regions), a possible caveat when comparing metallicities at different redshifts is the different aperture projected on the source. In particular, at high redshift spectroscopic observations are likely to sample most of the galaxy, while at low redshift and in local galaxies the spectroscopic aperture samples mostly the central higher metallicity region. This effect may mimic a metallicity evolution.

When comparing surveys at high redshifts this should be a minor issue, since the projected apertures on the sources are not

very different. At $z \sim 0.7$, the adopted aperture of 0.75–1.3” in Savaglio et al. (2005) corresponds to about 5.6–9.3 kpc; at $z \sim 2.2$ Erb et al. (2006) adopt an aperture of 0.76” corresponding to about 7.2 kpc. Our aperture of 0.75” at $z \sim 3.5$ corresponds to about 6 kpc.

However, aperture effects may be more serious for the local sample. At the median redshift of 0.07 the SDSS fiber size (3”) has a median size of 4 kpc, and a median covering factor $\sim 34\%$ relative to the total g’-band light, in contrast with a covering factor of $\sim 70\%$ at $z \sim 3.5$. The aperture effect is stronger for local high mass galaxies, which are generally bigger and for which the covering factor reach values as low as 20%. The problem of a differential aperture effect as a function of galaxy mass may also affect the shape of the local mass-metallicity relation, making the observed relation steeper than it actually is (Kewley & Ellison, 2008). However, the absolute magnitude of this effect in the local sample is estimated to be at most ~ 0.1 – 0.15 dex (Kewley & Ellison, 2008), which is significantly lower than the metallicity evolution observed at high redshift, at least at $z \sim 3.5$.

Additional issues related to aperture effects will be discussed in the context of the comparison with models in §7.5.

7.3. Selection effects

When comparing the mass-metallicity relation at $z \sim 3.5$ inferred from LBG’s with that inferred from local (or lower redshift) samples of star forming galaxies, one must be aware that we are comparing different classes of objects, which are not necessarily linked from an evolutionary point of view. As a consequence, the evolution of the mass-metallicity relation inferred in this paper should be regarded as the evolution of the mass-metallicity relation of galaxies representative of (or contributing significantly to) the density of star formation at each epoch, and *not* the evolutionary pattern of individual galaxies. This issue will be further discussed in the next sections. In this section we mostly investigate whether galaxies in our sample are representative of star forming galaxies at $z \sim 3.5$.

Stellar masses of LBGs at $z \sim 3$ were measured by Shapley et al. (2001)³, but for a subsample of galaxies about one magnitude brighter (in R-band) than the parent sample of Steidel et al. (2003). Shapley et al. (2001) obtain a median stellar mass of $2.4 \times 10^{10} M_\odot$. The galaxies in our sample (Tab. 2 and §6) have a median stellar mass of $\sim 1.6 \times 10^{10} M_\odot$, which is close to the value obtained by Shapley et al. (2001) for their large LBG sample. In any case, the distribution of stellar masses is not a concern, since the mass is one of the two variables that we are mapping on the mass-metallicity relation: even if we had a bias in terms of stellar mass, this would simply imply that we preferentially populate the diagram in a certain mass range, making the estimation of the mass-metallicity relation more uncertain in other mass ranges (because under-populated), but not biased.

Biases in terms of star formation rate are of a greater concern. Our selection requirement that sources must have a highly reliable spectroscopic redshift may bias our sample towards sources with strong UV continuum or strong Ly α , hence higher than average SFR. Tab. 2 shows the SFR inferred from the rest-frame UV continuum of the sources in our sample (see §6 for details), from which we infer a median SFR of $\sim 100 M_\odot \text{ yr}^{-1}$. This is similar to the median SFR ($90 M_\odot \text{ yr}^{-1}$) of LBGs at

² Note that, to avoid the fit to be dominated by the mass intervals with largest number of objects, we first obtained metallicity medians within mass bins and then fitted the resulting values with Eq. 2.

³ Note that Shapley et al. (2001) did not have access to Spitzer-IRAC data, and therefore their masses may be subject to significant uncertainties.

$z\sim 3$ obtained by Shapley et al. (2001) (who adopted a similar approach as ours to estimate the SFR from the UV continuum). However, since the latter work is biased towards slightly brighter optical magnitudes, the median SFR of the LBGs at $z\sim 3$ in the parent sample of Steidel et al. (2003) is probably somewhat lower. Since the median stellar masses are similar, then the specific star formation rate (SSFR) in our sample may be somewhat higher (up to a factor of 2) than in the LBG sample of Steidel et al. (2003). Ellison et al. (2008) investigated the effect of the SSFR on the metallicity in local galaxies. They found that, for a variation of the SSFR by a factor of two, the metallicity varies by less than ~ 0.1 dex in low mass galaxies ($M_* < 10^{10} M_\odot$), while no metallicity variations are found in massive galaxies ($M_* > 10^{10} M_\odot$). As a consequence, a possible bias of our sample in terms of SSFR relative to the LBG sample of Steidel et al. (2003) should not affect significantly the inferred mass-metallicity relation.

Another possible source of bias is that LBGs are selected through their UV rest-frame colors, hence they miss any population of heavily reddened star forming galaxies. Reddy et al. (2007) estimate that, due to this selection effect, LBG's represent $\sim 47\%$ of the population of star forming galaxies at $z\sim 3$ with $R < 25.5$ (see also Hopkins & Beacom, 2006). Dust reddened galaxies are naively expected to be more metal rich (since metallicity and dust content correlate, Hunt et al., 2005). On the contrary, Rupke et al. (2008) have shown that, at least at low- z , dusty galaxies (IR-selected) are characterized by gas metallicities lower than optical- and UV-selected galaxies (probably due to metal poor gas infalling from the outskirts in merging/interacting systems). Recently Caputi et al. (2008) have found a similar effect in dusty galaxies at intermediate redshift (i.e. metallicities lower than in optically selected galaxies). High- z dusty objects may behave differently. However, if the same phenomenon is also present at high- z , then LBG's would provide an upper limit to the metallicity of galaxies at $z\sim 3$. However, we do not speculate further on the properties of star forming galaxies that are not sampled by LBGs, and we simply emphasize that the results presented in this paper only apply to about half of the star forming galaxies at $z\sim 3$, i.e. those UV-selected.

7.4. The evolution of the mass-metallicity relation

The evolution of the mass-metallicity relation is summarized in Fig. 8, where we plot the best fits resulting from Eq. 2 both at $z\sim 3.5$ from the AMAZE survey, and at lower redshifts from previous surveys.

Figs. 7–8 highlights a clear evolution of the mass-metallicity relation of star forming galaxies through the cosmic epochs. As already discussed in §7.3, this evolution should *not* be seen as the evolutionary sequence of individual objects, since at each redshift the various surveys are sampling different classes of star forming galaxies, which are not necessarily each other progenitors. The trend observed in Figs. 7–8 should be regarded as the evolution of the mass-metallicity relation of galaxies dominating (or contributing significantly) the star formation density at each epoch.

At $M_* \sim 10^{10} M_\odot$ the metallicity at $z\sim 2.2$ is lower by a factor of about 2.5 with respect to local galaxies. Even if highly significant, such metallicity decrease is modest if one considers that from $z=0$ to $z=2.2$ the elapsed time is ~ 11 Gyr, i.e. about 75% of the age of the universe. From $z\sim 2.2$ to $z\sim 3.5$ the average metallicity of galaxies decreases by another factor of about 2.5. However, the latter evolution is much stronger, and faster.

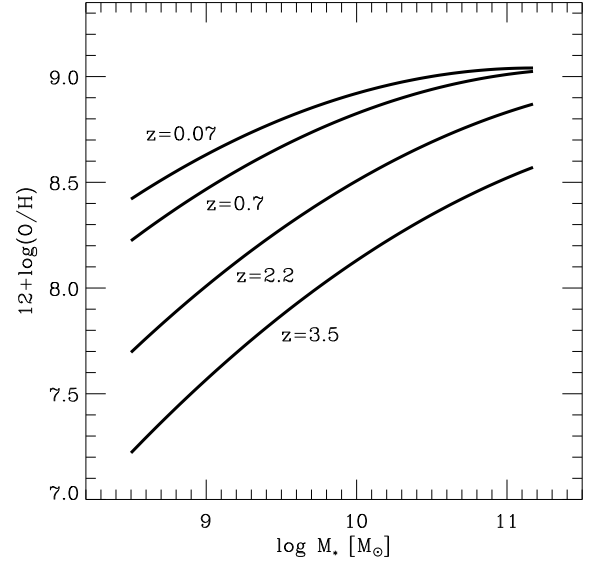


Fig. 8. Comparison of the mass-metallicity relation observed at different redshifts, as parametrized by the analytical function Eq. 2 and coefficients in Tab. 5.

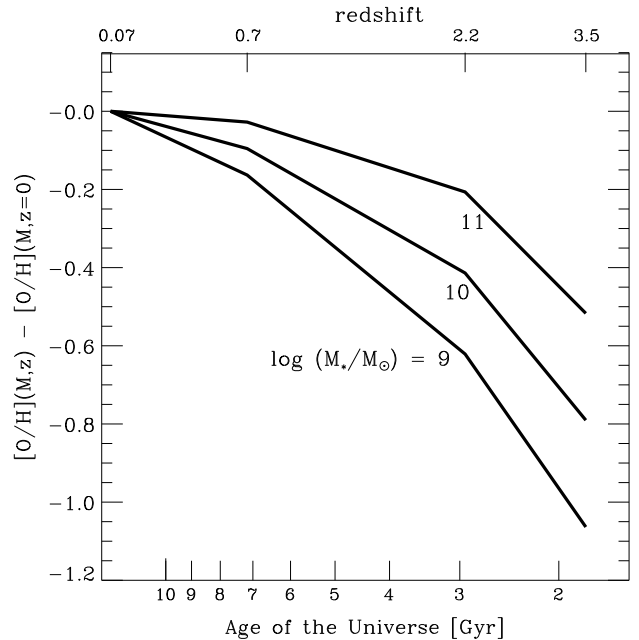


Fig. 9. Average metallicity of star forming galaxies as a function of the cosmic age of the Universe, relative to local galaxies, for three different families of galaxies with different stellar masses ($M_*/M_\odot = 10^9, 10^{10}, 10^{11}$). Ages are sampled at the redshifts where observations are directly available. The average metallicity for each stellar mass was inferred by using the parametrization given by Eq. 2 and Tab. 5.

Indeed, such a metallicity variation occurs on a much shorter time scale, only ~ 1 Gyr. This effect is shown in more clearly Fig. 9, where the the average metallicity of star forming galaxies is plotted as a function of the age of the universe, for different classes of galaxies with different stellar masses, by exploiting the analytical function in Eq. 2 (note that, as discussed above,

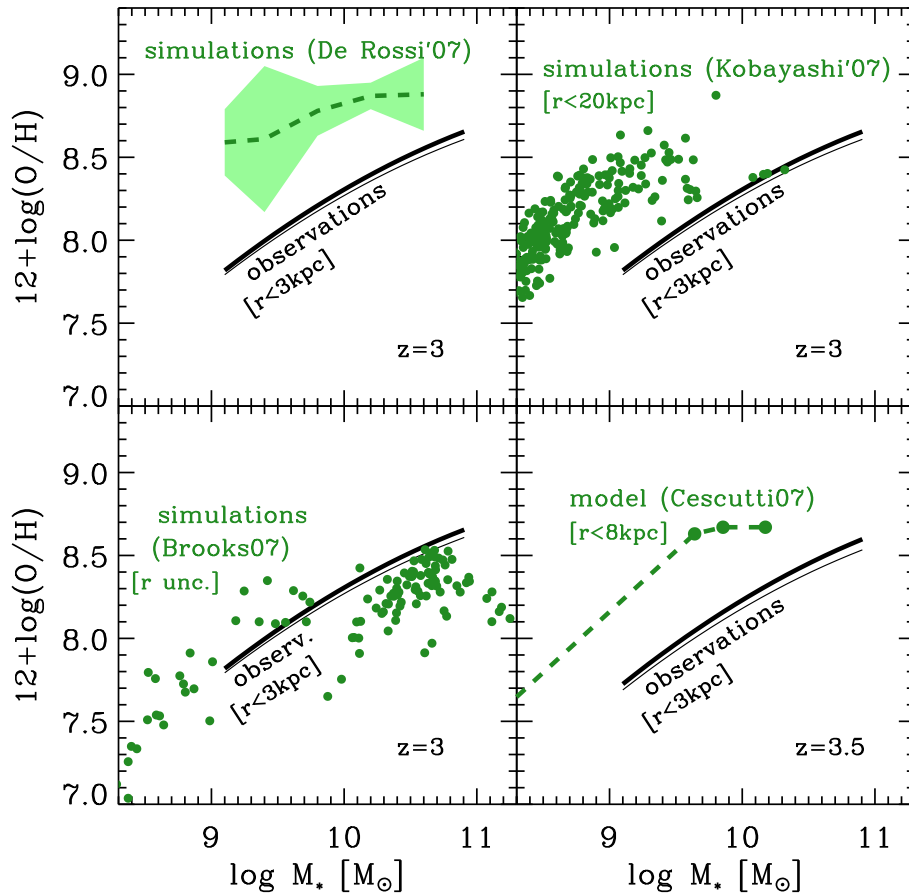


Fig. 10. Comparison between models/simulations predictions for the mass-metallicity relation at $z\sim 3$ and the results of our observations. The predictions obtained by models and simulations are shown with green points and dashed lines (the aperture used in the models/simulations is reported when available). The solid, black lines show the mass-metallicity relation observed at the same epochs (interpolated to the same, exact redshifts of the simulation by using Eq. 2 and Tab. 5). The thin black line shows the observed mass-metallicity relation by using the masses estimated with the BC03 templates, while the thick line is the inferred relation when using the M05 templates.

this figure does not provide the evolution of individual galaxies). We further note that the evolution is strong even in massive galaxies. Clearly, $z\sim 3.5$ is an epoch of major action for the evolution of galaxies, both in terms of star formation and chemical enrichment, even for massive systems.

We note that a similar strong evolution of the metallicities at $z>3$ was obtained by Mehlert et al. (2006) by investigating the *stellar* metallicities of a few galaxies with bright UV continuum. Their result was however affected by uncertainties on the absolute calibration of the stellar metallicity tracers. It is also interesting to note that the metallicities obtained by us at $z\sim 3.5$ are in fair agreement with those expected at the same redshift by Panter et al. (2008), who inferred the metallicity evolution of galaxies by modelling its “fossil” spectral signatures in local galaxies.

The additional interesting result is the indication of a differential, mass-dependent evolution of the metallicity. In particular, the metallicity evolution in low mass systems appears stronger than in massive galaxies (Figs. 7–9). This finding requires more statistics to be confirmed at $z\sim 3.5$ (to come with the completion of the AMAZE project). However, the evolution of the slope of the mass-metallicity relation (relative to the local slope) is significant even at $z\sim 0.7$ (as already noted by Savaglio et al., 2005; Kobulnicky et al., 2003) and at $z\sim 2.2$. A detailed investigation of differential selection effects as a function of stellar mass is re-

quired to rule out that observational biases are not affecting the slope of the mass-metallicity relation at each epoch. However, if confirmed, such mass-dependent evolution of the metallicity can be regarded as the “chemical” version of the galaxy downsizing: high mass galaxies reach high metallicities at high redshift, on short timescales, while low mass systems enrich their ISM over a prolonged period of time, extending to the current epoch.

7.5. Comparison with models of galaxy evolution

As mentioned in the introduction there is an intense theoretical activity aimed at interpreting the nature and origin of the mass-metallicity relation, and also at providing predictions on the expected mass-metallicity relation at high redshift. Comparing the models predictions with the observational results in a consistent way is not simple. Indeed, theoretical models predict a variety of galaxy populations, spanning a wide range of properties (e.g. in terms of SFR), while observations are limited to samples matching the survey selection criteria. Moreover, generally theoretical works provide the metallicity integrated over large apertures, including most of the galaxy, while observational metallicity measurements are generally obtained within a smaller aperture. In the future a collaborative effort with various theoretical groups is planned to match the outcome of models and simulations to the observational selection effects. However, a preliminary compar-

ison with the already published theoretical results is instructive to infer some initial constraints on galaxy evolutionary models.

Savaglio et al. (2005) interpreted the evolution of the mass–metallicity relation from $z \sim 2.2$ to $z=0$ through a closed-box model with an exponentially decaying SFR $\propto e^{-t/\tau}$, where the e -folding time τ decreases as a function of galaxy mass. However the inclusion of our data at $z \sim 3.5$ makes this model not suitable. It is difficult to simultaneously fit the observed mass–metallicity relations at $z=0.1$, $z=0.7$, $z=2.2$ and $z=3.5$ with a simple closed-box model, unless more complex scenarios of the SF history are envisaged. Moreover, an exponentially decaying SFR, with the e -folding times provided by Savaglio et al. (2005) makes the SFR extrapolated to local massive systems well below $1 M_{\odot} \text{ yr}^{-1}$, i.e. these should be local quiescent galaxies (probably massive elliptical), which cannot be representative of the local star forming galaxies used to derive the local mass–metallicity relation in Tremonti et al. (2004) and Kewley & Ellison (2008). Finally, it is unlikely that the closed-box scenario applies to LBGs, which are characterized by strong, unbound winds (e.g. Pettini et al., 2002).

Within the framework of the hierarchical models of galaxy evolution, de Rossi et al. (2007) performed numerical hydrodynamical simulations enabling them to provide detailed predictions on the evolution of the mass–metallicity relation at various epochs. In the top-left panel of Fig. 10 the dashed green line shows the mass–metallicity relation predicted at $z=3$ by the simulations of de Rossi et al. (2007) (therein Tab. 3), while the shaded areas give the dispersion inferred from the same simulations (note that de Rossi et al., 2007, use the same IMF adopted by us, therefore no further correction is required). Since we do not have the observational data at exactly the same epoch of the simulations ($z=3$), we interpolate the observed mass–metallicity to the same epoch of the simulations by using Eq. 2 and Tab. 5. The *observed* mass–metallicity relation at $z=3$ is shown in Fig. 10 with a thin, black solid line. We also show the mass–metallicity relation inferred by adopting the stellar masses measured with the M05 templates (thick solid line). Fig. 10 shows a significant discrepancy between simulations and observations. The discrepancy was also present at $z=2$ (although at a lower level), as noted by de Rossi et al. (2007). They suggest that the inconsistency between simulations and observations is due to the lack of significant SN feedback in their simulations, which would remove metal enriched gas and lower the global gas metallicity.

However, the discrepancy with observations is present also for simulations that include the effect of SN feedback. This is the case of the hierarchical, three-dimensional chemodynamical simulations presented in Kobayashi et al. (2007), which include the feedback from SNII and hypernovae. They provide predictions of the mass–metallicity relation as a function of redshift. The green points in the top-right panel of Fig. 10 show the results of such simulations at $z=3$ (also Kobayashi et al., 2007, use the same IMF adopted by us, therefore no further correction is required). Even in this case there is a discrepancy between simulations and observations. The discrepancy is much reduced with respect to the de Rossi et al. (2007) simulations, but still significant at low masses ($\log(M_{*}/M_{\odot}) < 10$). At high masses ($\log(M_{*}/M_{\odot}) \sim 10.5$) simulations and observations are nearly consistent. However, one should take into account that Kobayashi et al. (2007) extract the metallicities in the simulated galaxies within a radius of $r < 20 \text{ kpc}$, i.e. by including metal poor external regions, while observations provide metallicities within a radius of $r < 3 \text{ kpc}$. Aperture effects are probably more important in large, massive galaxies. If the extraction radius of

the simulations is matched to the observations then the discrepancy probably increases strongly also in the high mass region.

The main problem of the latter simulations seems to be that the bulk of the chemical enrichment occurs in small galaxies, yielding a steep metallicity evolution at masses below $< 10^9 M_{\odot}$ on the mass–metallicity plane. Then such evolved sub-units merge to form massive systems, with little additional star formation (close-to-dry merging), implying little additional enrichment (i.e. flatter evolution towards high masses). The discrepancy with the observations seems to imply that the evolution of galaxies at high redshift occurs through the assembly of little evolved small galaxies, so that high- z objects with $\log(M_{*}/M_{\odot}) > 9$ can exist with relatively low metallicities. In these systems most of the star formation and chemical evolution occurs once they are already assembled into bigger systems.

The latter scenario is well described by the simulations presented in Governato et al. (2007), which model the evolution of disks within a hierarchical framework. In these simulations a strong feedback, due to SNe and to gas heating by the UV radiation, prevents small galaxies to evolve significantly before merging into a bigger galaxy, while the bulk of the chemical evolution and star formation occurs in the gas which has already settled into the proto-disk. Brooks et al. (2007) inferred the evolution of the mass–metallicity relation from these simulations, whose prediction at $z=3$ is shown in the bottom-left panel of Fig. 10 (Brooks, priv. comm.). The agreement with the observations is good, although at high masses the simulations tend to under-reproduce the observed metallicity. However the metallicities provided by Brooks et al. (2007) are obtained without any constraints on the aperture (i.e. all cold gas); if the information from the simulated galaxies is extracted within our observational aperture ($r < 3 \text{ kpc}$) then metallicities are expected to increase (especially in large massive galaxies) and better reproduce the observations. Yet, a potential problem of the Governato et al. (2007) and Brooks et al. (2007) models is that their forming disks are characterized by modest star formation rates, never exceeding $\sim 20 M_{\odot} \text{ yr}^{-1}$, while LBGs (except for a minority of them) are characterized by significantly larger SFR, suggesting that they are in the process of rapidly forming spheroids.

Detailed predictions on the mass–metallicity relation were also obtained by Finlator & Davé (2008) who used three-dimensional hierarchical simulations along with detailed out-flows models. They show that the evolution of the mass–metallicity relation out to $z \sim 2$ can be well reproduced if a “momentum-driven wind” model is incorporated. The predictions of their model at $z \sim 3$ reproduce reasonably well also the metallicity in massive galaxies ($\log(M_{*}/M_{\odot}) \sim 10.5$) observed by us. However, their model predicts an up-turn of the mass–metallicity slope at $z \sim 3$ which is not observed by us. Yet, the slope of the mass–metallicity relation is still poorly determined in our data, due to the shortage of low-mass galaxies; we should wait for the completion of the AMAZE program before claiming any significant inconsistency with the model in terms of slope of the relation.

In the bottom-right diagram of Fig. 10 we also show the mass–metallicity relation expected by the double-infall models for the formation of galactic disks and dwarfs presented in Chiappini et al. (2001) and Cescutti et al. (2007). The green points show the mass–metallicity relation of spirals according to these models, by tracing back their evolution until $z=3.5$. The figure shows a significant discrepancy between the model and the observations. Such a discrepancy is not surprising, since LBG’s at $z > 2$ are probably spheroids in the process of rapidly forming stars, and not spirals. More specifically, in the double-

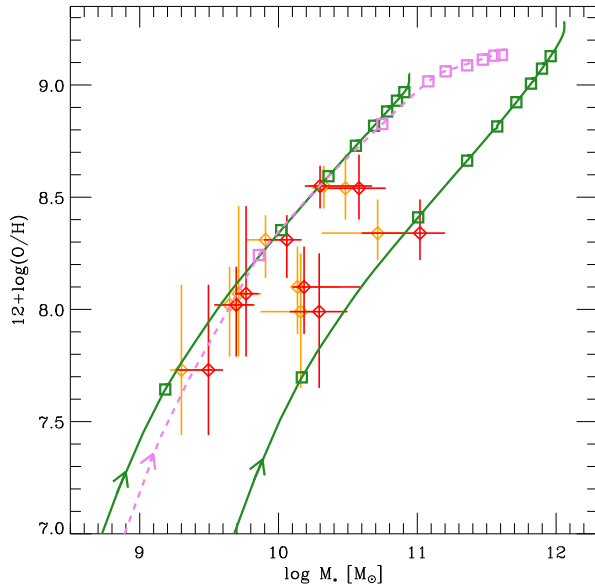


Fig. 11. Evolutionary tracks of *individual* galaxies on the mass-metallicity diagram according to some models for the formation of spheroids presented in Granato et al. (2004) (green solid lines) and in Pipino et al. (2006) (violet dashed lines), compared with the mass-metallicity relation observed at $z\sim 3.5$ (diamonds with errorbars). Squares mark the models temporal evolution from 0.02 Gyr to 0.3 Gyr, in steps of 0.04 Gyr. Red symbols show the masses of the observed objects inferred with the BC03 templates, while orange symbols are the masses inferred with the M05 templates.

infall model for disks the star formation rate never exceeds a few times $10 M_{\odot} \text{ yr}^{-1}$, while the median SFR of LBGs is $90 M_{\odot} \text{ yr}^{-1}$.

Summarizing, there are currently no models or simulations that can satisfactorily explain the mass-metallicity relation observed at $z\sim 3$. The closest match is probably with the simulations of Governato et al. (2007) and Brooks et al. (2007), although even in these cases there are some discrepancies in terms of SFR. The location of LBGs at $z\sim 3$ on the mass-metallicity plane, along with comparison with these models, suggest that $z\sim 3$ galaxies have been assembled through low mass systems whose star formation efficiency was suppressed, hence which were little evolved. The bulk of the star formation and of the chemical enrichment occurred once small galaxies were already assembled into bigger systems. In other words, most of the merging occurred before most of the star formation.

We conclude this section by comparing in Fig. 11 the location of $z\sim 3.5$ galaxies on the mass-metallicity diagram with the evolutionary tracks (as a function of time) expected for individual spheroidal galaxies, according to the models in Granato et al. (2004) and Pipino et al. (2006). These models prescribe a nearly monolithic formation of elliptical galaxies, where pristine gas collapses from the halo. In these models star formation is gradually quenched as the galaxy evolves due to the feedback introduced by star formation and/or AGN activity. The mass-metallicity tracks of these models are shown in Fig. 11 for different final stellar masses: green solid lines and violet dashed line are for the Granato et al. (2004) model and for the Pipino et al. (2006) model, respectively. The observational data from the Amaze project are shown with diamonds and errorbars. Red

points are for masses inferred by using the BC03 templates, orange points are for masses inferred by using the M05 templates. The models can easily embrace the observed data points. This comparison is not aimed at explaining the mass-metallicity relation at $z\sim 3.5$, since models of individual galaxies at different masses must be convolved with the evolution of cosmic structures to obtain a prediction of the mass-metallicity relation at any epoch. Nonetheless, Fig. 11 shows that the combination of mass and metallicities observed in individual star forming galaxies at $z\sim 3.5$ does not lie in a region difficult to populate by models of individual galaxies; on the contrary, individual observations can be easily explained in terms of rapidly evolving, massive systems, through these simple models. However, convolving these models with the hierarchical growth of dark matter structures is required to verify whether they can really explain the mass-metallicity relation at $z\sim 3.5$.

8. Summary and conclusions

We have presented initial results of the AMAZE project, an ESO large programme aimed at determining the mass-metallicity relation of star forming galaxies at $z>3$. Near-IR spectra are being obtained with SINFONI, the VLT near-IR integral field spectrometer, for a sample of Lyman Break Galaxies at $3<z<5$.

Gas metallicities are inferred by using a combination of diagnostics involving nebular lines observable in the H and K bands. To have a metallicity scale consistent with the results obtained by previous surveys at lower redshifts, we derived new accurate calibrations of various strong-line metallicity diagnostics spanning the wide range $7.1 < 12 + \log(\text{O}/\text{H}) < 9.1$.

AGNs (which would affect and make unusable the metallicity diagnostics) were carefully removed through a multiwavelength approach using X-ray, optical and mid-IR data. In particular, the use of mid-IR (Spitzer-MIPS) data allows us to discard even heavily obscured, Compton thick AGNs.

Stellar masses are inferred by fitting multi-band photometric data with galaxy templates. Within this context crucial is the use of Spitzer-IRAC data, which sample the rest-frame near-IR stellar light at $3<z<5$.

In this paper we have presented results from an initial sample of 9 LBGs at $3.1<z<3.7$. Emission lines required to constrain the gas metallicity are detected in all sources. From the mass-metallicity relation at $z\sim 3.5$ inferred from this initial sample we obtain the following results:

1. When compared with the results of previous surveys at lower redshift (recalibrated to match our metallicity and mass calibrations), we obtain evidence for a clear evolution of the mass-metallicity relation as a function of redshift. Since at different redshifts we are sampling different populations of galaxies, the observed evolution should *not* be considered the evolutionary pattern of individual galaxies, but as the evolution of the mass-metallicity relation of the dominant population of star forming galaxies at each epoch. The evolution of the mass-metallicity relation is faster at $2.2<z<3.5$ than at later epochs ($z<2.2$). This result indicates that $z\sim 3$ is an epoch of major action for the enrichment of galaxies, even in high mass systems
2. There are indications that the metallicity evolution is not constant with mass: low mass galaxies evolve more strongly than massive systems. If confirmed, this result can be considered as the chemical version of the galaxy downsizing, i.e. a scenario where high mass galaxies reach high metallicities at high redshift, on short timescales, while low mass systems

enrich their ISM over a prolonged period of time, extending to the current epoch. However, this finding is subject to uncertainties due to low statistics at low masses, and must await additional data to be confirmed.

3. The observed mass-metallicity relation at $z\sim 3$ is difficult to reconcile with the simulations by some hierarchical models, which predict metallicities higher than observed. If aperture effects are taken into account then the discrepancy is probably even higher. The main problem of these models seems to be that galaxies are assembled once they are already evolved, from the stellar and chemical point of view. Our results suggest that galaxies at $z>3$ are assembled mostly with relatively un-evolved small galaxies, whose star formation efficiency is low. Most of the chemical evolution (hence most of the star formation) must occur once small galaxies are already assembled into bigger ones. This implies that most of the merging occurs before most of the star formation. Indeed, models and simulations where a strong feedback keeps star formation low in the assembling small galaxies (preventing them to evolve strongly from the stellar and chemical point of view), provide a much better description of the mass-metallicity relation at $z\sim 3.5$.

The finding that galaxies at $z>3$ are mostly assembled with un-evolved sub-units is not necessarily in contrast with models of “dry-merging”, i.e. models where galaxy assembly occurs through systems that are significantly evolved and with little residual gas. Indeed, dry merging may be the main mode of galaxy evolution at lower redshifts ($z<3$) without being in conflict with our findings at $z>3$.

Acknowledgements. We thank A. Modigliani for his assistance in using the SINFONI pipeline. We are grateful to C. Kobayashi, S. Savaglio and A. Brooks for providing us the electronic version of their simulations and data. We thank M.E. De Rossi for useful comments. Part of this work was supported by the Italian Institute for Astrophysics (INAF) and by the Italian Space Agency (ASI) through contract ASI-INAF I/016/07/0.

References

- Allende Prieto, C., Lambert, D. L., & Asplund, M. 2001, *ApJ*, 556, L63
- Alonso-Herrero, A., et al. 2006, *ApJ*, 640, 167
- Akerman, C. J., Ellison, S. L., Pettini, M., & Steidel, C. C. 2005, *A&A*, 440, 499
- Asari, N. V., Cid Fernandes, R., Stasińska, G., Torres-Papaqui, J. P., Mateus, A., Sodré, L., Schoenell, W., & Gomes, J. M. 2007, *MNRAS*, 381, 263
- Baldwin, J. A., Phillips, M. M., & Terlevich, R. 1981, *PASP*, 93, 5
- Bouché, N., Lehnert, M. D., & Péroux, C. 2006, *MNRAS*, 367, L16
- Bouché, N., Lehnert, M. D., Aguirre, A., Péroux, C., & Bergeron, J. 2007, *MNRAS*, 378, 525
- Bresolin, F. 2006a, *ArXiv Astrophysics e-prints*, arXiv:astro-ph/0608410
- Bresolin, F., Pietrzyński, G., Urbaneja, M. A., Gieren, W., Kudritzki, R.-P., & Venn, K. A. 2006b, *ApJ*, 648, 1007
- Bresolin, F. 2007a, *ApJ*, 656, 186
- Bresolin, F., Urbaneja, M. A., Gieren, W., Pietrzyński, G., & Kudritzki, R.-P. 2007b, *ApJ*, 671, 2028
- Brinchmann, J., Pettini, M., & Charlot, S. 2008, *MNRAS*, 198
- Brodie, J. P., & Huchra, J. P. 1991, *ApJ*, 379, 157
- Brooks, A. M., Governato, F., Booth, C. M., Willman, B., Gardner, J. P., Wadsley, J., Stinson, G., & Quinn, T. 2007, *ApJ*, 655, L17
- Bruzual, G., & Charlot, S. 2003, *MNRAS*, 344, 1000 (BC03)
- Calzetti, D., Armus, L., Bohlin, R. C., Kinney, A. L., Koornneef, J., & Storchi-Bergmann, T. 2000, *ApJ*, 533, 682
- Caputi, K. I., et al. 2008, *ArXiv e-prints*, 803, arXiv:0803.1002
- Cardelli, J. A., Clayton, G. C., & Mathis, J. S. 1989, *ApJ*, 345, 245
- Cescutti, G., Matteucci, F., François, P., & Chiappini, C. 2007, *A&A*, 462, 943
- Cid Fernandes, R., Asari, N. V., Sodré, L., Stasińska, G., Mateus, A., Torres-Papaqui, J. P., & Schoenell, W. 2007, *MNRAS*, 375, L16
- Chiappini, C., Matteucci, F., & Romano, D. 2001, *ApJ*, 554, 1044
- Daddi, E., et al. 2007, *ApJ*, in press, arXiv:0705.2832v2
- Dalcanton, J. J. 2007, *ApJ*, 658, 941
- Davé, R., & Oppenheimer, B. D. 2007, *MNRAS*, 374, 427
- Davies, R. I. 2007, *MNRAS*, 375, 1099
- De Lucia, G., Kauffmann, G., & White, S. D. M. 2004, *MNRAS*, 349, 1101
- de Mello, D. F., Daddi, E., Renzini, A., Cimatti, A., di Serego Alighieri, S., Pozzetti, L., & Zamorani, G. 2004, *ApJ*, 608, L29
- de Rossi, M. E., Tissera, P. B., & Scannapieco, C. 2007, *MNRAS*, 374, 323
- Dickinson, M., Papovich, C., Ferguson, H.C., Budavari, T. 2003, *ApJ*, 587, 25
- Dopita, M. A., & Sutherland, R. S. 1996, *ApJS*, 102, 161
- Dopita, M. A., et al. 2006, *ApJS*, 167, 177
- Drory, N., Bender, R., Feulner, G., et al. 2004, *ApJ*, 608, 742
- Eisenhauer, F., et al. 2003, *Proc. SPIE*, 4841, 1548
- Ellison, S. L., Patton, D. R., Simard, L., & McConnachie, A. W. 2008, *ApJ*, 672, L107
- Erb, D. K., Steidel, C. C., Shapley, A. E., Pettini, M., Reddy, N. A., & Adelberger, K. L. 2006, *ApJ*, 646, 107
- Feulner, G., Gabasch, A., Salvato, M., Drory, N., Hopp, U., & Bender, R. 2005, *ApJ*, 633, L9
- Finlator, K., & Davé, R. 2008, *MNRAS*, 385, 2181
- Fiore, F., et al. 2007, *ApJ*, in press, arXiv:0705.2864v2
- Fontana, A., et al. 2006, *A&A*, 459, 745
- Förster Schreiber, N. M., et al. 2006, *ApJ*, 645, 1062
- Franceschini, A., et al. 2006, *A&A*, 453, 397
- Frye, B., Broadhurst, T., & Benítez, N. 2002, *ApJ*, 568, 558
- Frye, B. L., et al. 2007, *ApJ*, 665, 921
- Gallazzi, A., Charlot, S., Brinchmann, J., & White, S. D. M. 2006, *MNRAS*, 370, 1106
- Garnett, D. R., & Shields, G. A. 1987, *ApJ*, 317, 82
- Garnett, D. R., et al. 2004, *ApJ*, 607, L21
- Governato, F., Willman, B., Mayer, L., Brooks, A., Stinson, G., Valenzuela, O., Wadsley, J., & Quinn, T. 2007, *MNRAS*, 374, 1479
- Granato, G. L., De Zotti, G., Silva, L., Bressan, A., & Danese, L. 2004, *ApJ*, 600, 580
- Grazian, A., et al. 2006, *A&A*, 449, 951
- Grazian, A., et al. 2007, *A&A*, 465, 393
- Halliday, C., et al. submit.
- Hao, L., et al. 2005, *AJ*, 129, 1783
- Hopkins, A. M., & Beacom, J. F. 2006, *ApJ*, 651, 142
- Hunt, L., Bianchi, S., & Maiolino, R. 2005, *A&A*, 434, 849
- Juneau, S., et al. 2005, *ApJ*, 619, L135
- Kennicutt, R. C., Jr., Bresolin, F., & Garnett, D. R. 2003, *ApJ*, 591, 801
- Kewley, L. J., & Dopita, M. A. 2002, *ApJS*, 142, 35
- Kewley, L. J., & Ellison, S. L. 2008, *ArXiv e-prints*, 801, arXiv:0801.1849
- Kobayashi, C., Springel, V., & White, S. D. M. 2007, *MNRAS*, 376, 1465
- Kobulnicky, H. A., & Koo, D. C. 2000, *ApJ*, 545, 712
- Kobulnicky, H. A., et al. 2003, *ApJ*, 599, 1006
- Kobulnicky, H. A., & Kewley, L. J. 2004, *ApJ*, 617, 240
- Köppen, J., Weidner, C., & Kroupa, P. 2007, *MNRAS*, 375, 673
- Kroupa, P. 2001, *MNRAS*, 322, 231
- Kulkarni, V. P., Fall, S. M., Lauroesch, J. T., York, D. G., Welty, D. E., Khare, P., & Truran, J. W. 2005, *ApJ*, 618, 68
- Ledoux, C., Petitjean, P., Fynbo, J. P. U., Møller, P., & Srianand, R. 2006, *A&A*, 457, 71
- Lequeux, J., Peimbert, M., Rayo, J. F., Serrano, A., & Torres-Peimbert, S. 1979, *A&A*, 80, 155
- Liang, Y. C., Hammer, F., & Flores, H. 2006, *A&A*, 447, 113
- Liang, Y. C., et al. 2007, *A&A*, 473, 411
- Liu, X., Shapley, A. E., Coil, A. L., Brinchmann, J., & Ma, C.-P. 2008, *ArXiv e-prints*, 801, arXiv:0801.1670
- Maier, C., Meisenheimer, K., & Hippelein, H. 2004, *A&A*, 418, 475
- Maier, C., Lilly, S. J., Carollo, C. M., Stockton, A., & Brodwin, M. 2005, *ApJ*, 634, 849
- Maier, C., Lilly, S. J., Carollo, C. M., Meisenheimer, K., Hippelein, H., & Stockton, A. 2006, *ApJ*, 639, 858
- Maiolino, R., Rieke, G. H., & Rieke, M. J. 1996, *AJ*, 111, 537
- Maiolino, R., et al. 2003, *MNRAS*, 344, L59
- Maiolino, R., et al. 2007a, in “A Century of Cosmology: Past, Present and Future” (Venezia, August 2007), *ArXiv e-prints*, 712, arXiv:0712.2880
- Maiolino, R., et al. in “Formation and evolution of galaxy disks” (Rome, October 2007)
- Maraston, C., 2005, *MNRAS*, 362, 799 (M05)
- Martínez-Sansigre, A., Rawlings, S., Lacy, M., Fadda, D., Jarvis, M. J., Marleau, F. R., Simpson, C., & Willott, C. J. 2006, *MNRAS*, 370, 1479
- Martínez-Sansigre, A., et al. 2007, *MNRAS*, 379, L6
- Matteucci, F. 1994, *A&A*, 288, 57
- Mehlert, D., Tapken, C., Appenzeller, I., Noll, S., de Mello, D., & Heckman, T. M. 2006, *A&A*, 455, 835
- Nesvadba, N. P. H., et al. 2006, *ApJ*, 650, 661
- Nagao, T., Maiolino, R., & Marconi, A. 2006, *A&A*, 459, 85
- Panther, B., et al. 2008, *MNRAS*, *submit.* arXiv:0804.3091v1
- Perez-Gonzalez, P. G., et al. 2007, *ArXiv e-prints*, 709, arXiv:0709.1354

- Pettini, M., Shapley, A. E., Steidel, C. C., Cuby, J.-G., Dickinson, M., Moorwood, A. F. M., Adelberger, K. L., & Giavalisco, M. 2001, *ApJ*, 554, 981
- Pettini, M., Rix, S. A., Steidel, C. C., Adelberger, K. L., Hunt, M. P., & Shapley, A. E. 2002, *ApJ*, 569, 742
- Pettini, M., & Pagel, B. E. J. 2004, *MNRAS*, 348, L59
- Pickles, A. J. 1998, *PASP*, 110, 863
- Pilyugin, L. S. 2001, *A&A*, 374, 412
- Pipino, A., Matteucci, F., & Chiappini, C. 2006, *ApJ*, 638, 739
- Polletta, M. d. C., et al. 2006, *ApJ*, 642, 673
- Polletta, M., et al. 2007, *ApJ*, 663, 81
- Pozzetti, L., et al. 2007, *A&A*, 474, 443
- Pozzi, F., et al. 2007, *A&A*, 468, 603
- Prochaska, J. X., Gawiser, E., Wolfe, A. M., Castro, S., & Djorgovski, S. G. 2003, *ApJ*, 595, L9
- Prochaska, J. X., et al. 2007, *ApJ*, submit., arXiv:astro-ph/0703701v1
- Reddy, N. A., Steidel, C. C., Pettini, M., Adelberger, K. L., Shapley, A. E., Erb, D. K., & Dickinson, M. 2007, *ArXiv e-prints*, 706, arXiv:0706.4091
- Rix, S. A., Pettini, M., Leitherer, C., Bresolin, F., Kudritzki, R.-P., & Steidel, C. C. 2004, *ApJ*, 615, 98
- Rola, C. S., Terlevich, E., & Terlevich, R. J. 1997, *MNRAS*, 289, 419
- Rupe, D.S.N., et al. 2008, *ApJ*, in press (arXiv:0708.1766)
- Savaglio, S., et al. 2005, *ApJ*, 635, 260
- Shapley, A. E., Steidel, C. C., Adelberger, K. L., Dickinson, M., Giavalisco, M., & Pettini, M. 2001, *ApJ*, 562, 95
- Shapley, A. E., Erb, D. K., Pettini, M., Steidel, C. C., & Adelberger, K. L. 2004, *ApJ*, 612, 108
- Shapley, A. E., Coil, A. L., Ma, C.-P., & Bundy, K. 2005, *ApJ*, 635, 1006
- Skillman, E. D., Kennicutt, R. C., & Hodge, P. W. 1989, *ApJ*, 347, 875
- Spergel, D. N., et al. 2003, *ApJS*, 148, 175
- Stasińska, G. 2005, *A&A*, 434, 507
- Steidel, C. C., Adelberger, K. L., Shapley, A. E., Pettini, M., Dickinson, M., & Giavalisco, M. 2003, *ApJ*, 592, 728
- Tassis, K., Kravtsov, A. V., & Gnedin, N. Y. 2008, *ApJ*, 672, 888
- Tissera, P. B., De Rossi, M. E., & Scannapieco, C. 2005, *MNRAS*, 364, L38
- Tremonti, C. A., et al. 2004, *ApJ*, 613, 898
- Vanzella, E., et al. 2006, *A&A*, 454, 423
- Veilleux, S., & Osterbrock, D. E. 1987, *ApJS*, 63, 295
- Yin, S. Y., Liang, Y. C., Hammer, F., Brinchmann, J., Zhang, B., Deng, L. C., & Flores, H. 2007, *A&A*, 462, 535
- Zaritsky, D., Kennicutt, R. C., Jr., & Huchra, J. P. 1994, *ApJ*, 420, 87

Table 1. Photometric properties and integration times of the AMAZE sub-sample presented here

Name	RA(J2000)	Dec(J2000)	z	R _{AB}	[3.6 μ m] _{AB}	[24 μ m] _{AB}	T _{int}
CDFa-C9	00 53 13.7	+12 32 11.1	3.2119	23.99	22.66	>19.3	3.3
CDFS-4414	03 32 23.2	-27 51 57.9	3.4714	24.18	22.99	20.7	6.7
CDFS-4417	03 32 23.3	-27 51 56.8	3.4733	23.42	22.23	>19.9	6.7
CDFS-6664	03 32 33.3	-27 50 07.4	3.7967	24.80	25.26	>19.9	5.0
CDFS-16767	03 32 35.9	-27 41 49.9	3.6241	24.13	24.04	>19.9	7.5
CDFS-11991	03 32 42.4	-27 45 51.6	3.6110	24.23	23.91	>19.9	7.5
CDFS-2528	03 32 45.5	-27 53 33.3	3.6877	24.64	24.17	>19.9	4.2
SSA22a-M38	22 17 17.7	+00 19 00.7	3.2940	24.11	21.75 ^a	>19.6	6.7
SSA22a-aug16M16	22 17 30.8	+00 13 10.7	3.2920	23.83	22.87	>19.8	4.2

The following quantities are reported in each column: col. 1, object name; cols. 2-3, coordinates (J2000); col. 4, redshift spectroscopically determined through the [OIII]5007 line in our spectra; col. 5, R-band AB-magnitude; col. 6, Spitzer-IRAC 3.6 μ m AB magnitude; col. 7, Spitzer-MIPS 24 μ m AB magnitude (lower limits are at 3σ); col.8, on-source integration time (in unit of hours).

Note: ^a This is the AB magnitude at 4.5 μ m, since photometry at 3.6 μ m is not available.

Table 2. Physical properties of the sample inferred from their SED

Name	logM _* (BC03) [M _⊙]	logM _* (M05) [M _⊙]	M _B [mag]	U–V [mag]	SFR [M _⊙ yr ⁻¹]	E(B–V) _* [mag]	age [Gyr]
CDFa-C9	10.18 ^{+0.40} _{-0.08}	10.13 ^{+0.30} _{-0.05}	-22.36	-0.24	265	0.25 ^{+0.05} _{-0.10}	0.06 ^{+0.25} _{-0.01}
CDFS-4414	10.57 ^{+0.19} _{-0.22}	10.48 ^{+0.06} _{-0.23}	-22.47	-0.02	113	0.20 ^{+0.05} _{-0.10}	0.39 ^{+0.60} _{-0.29}
CDFS-4417	10.29 ^{+0.37} _{-0.11}	10.32 ^{+0.29} _{-0.10}	-22.79	-0.35	438	0.25 ^{+0.05} _{-0.10}	0.05 ^{+0.23} _{-0.99}
CDFS-6664	9.49 ^{+0.10} _{-0.23}	9.30 ^{+0.22} _{-0.08}	-20.93	-0.70	35	0.10 ^{+0.10} _{-0.04}	0.10 ^{+0.09} _{-0.05}
CDFS-16767	10.05 ^{+0.10} _{-0.16}	9.90 ^{+0.13} _{-0.13}	-21.90	-0.49	84	0.15 ^{+0.05} _{-0.05}	0.12 ^{+0.07} _{-0.07}
CDFS-11991	9.69 ^{+0.12} _{-0.15}	9.64 ^{+0.18} _{-0.08}	-21.64	-0.46	55	0.10 ^{+0.05} _{-0.04}	0.10 ^{+0.09} _{-0.05}
CDFS-2528	9.76 ^{+0.09} _{-0.07}	9.71 ^{+0.16} _{-0.00}	-21.57	-0.33	101	0.20 ^{+0.05} _{-0.05}	0.06 ^{+0.03} _{-0.01}
SSA22a-M38	11.01 ^{+0.18} _{-0.41}	10.71 ^{+0.19} _{-0.40}	-22.99	0.22	115	0.20 ^{+0.05} _{-0.20}	0.63 ^{+0.95} _{-0.45}
SSA22a-aug16M16	10.29 ^{+0.20} _{-0.21}	10.15 ^{+0.11} _{-0.28}	-22.32	-0.23	42	0.06 ^{+0.04} _{-0.06}	0.39 ^{+0.39} _{-0.23}

The following quantities are reported in each column: col. 1, object name; col. 2, stellar mass inferred by using the galaxy templates of BC03; col. 3, stellar mass inferred by using the galaxy templates of M05; col. 4, absolute B magnitude; col. 5, rest-frame U–V color; col. 6, star formation rate (by using BC03); col. 7, dust reddening affecting the stellar light, by using the attenuation curve of Calzetti et al. (2000); col. 8, age of the stellar population.

Table 3. Line fluxes and metallicities inferred from the near-IR spectra

Name	F([OIII]5007)	F(H β)	F([OII]3727)	F([NeIII]3870)	12+log(O/H)
		10 ⁻¹⁷ erg s ⁻¹ cm ^{-2a}			
CDFa-C9	6.83 \pm 0.21	1.44 \pm 0.18	2.16 \pm 0.14	0.53 \pm 0.13	8.10 ^{+0.18} _{-0.71}
CDFS-4414	0.95 \pm 0.11	0.40 \pm 0.10	0.87 \pm 0.08	<0.20	8.54 ^{+0.15} _{-0.14}
CDFS-4417	2.00 \pm 0.11	0.89 \pm 0.09	1.17 \pm 0.11	0.20 \pm 0.09	8.55 ^{+0.09} _{-0.10}
CDFS-6664	2.71 \pm 0.20	0.50 \pm 0.16	0.40 \pm 0.07	–	7.73 ^{+0.38} _{-0.29}
CDFS-16767	1.90 \pm 0.14	0.50 \pm 0.10	0.50 \pm 0.06	–	8.31 ^{+0.11} _{-0.17}
CDFS-11991	2.94 \pm 0.11	0.26 \pm 0.10	0.62 \pm 0.08	0.15 \pm 0.08	8.02 ^{+0.17} _{-0.23}
CDFS-2528	1.87 \pm 0.26	0.32 \pm 0.18	0.67 \pm 0.16	–	8.07 ^{+0.39} _{-0.28}
SSA22a-M38	5.41 \pm 0.31	1.48 \pm 0.20	3.51 \pm 0.37	<0.70	8.34 ^{+0.15} _{-0.12}
SSA22a-aug16M16	1.65 \pm 0.10	0.30 \pm 0.07	0.45 \pm 0.11	<0.25	7.99 ^{+0.26} _{-0.34}
Composite ^a	4.58 \pm 0.12	1.00 \pm 0.10	1.50 \pm 0.14	0.25 \pm 0.12	8.24 ^{+0.15} _{-0.20}

The following quantities are reported in each column: col. 1, object name; col. 2-5, emission line fluxes; col. 6, gas metallicity.

Notes: ^a In the case of the composite spectrum fluxes are normalized to the H β flux (which is also subject to an error as listed in the corresponding column).

Table 4. Coefficients for different strong-line metallicity diagnostics in Eq. 1.

Flux ratio (log R)	c ₀	c ₁	c ₂	c ₃	c ₄
log R ₂₃ ^a	0.7462	-0.7149	-0.9401	-0.6154	-0.2524
log [F([NII]6584)/F(H α)]	-0.7732	1.2357	-0.2811	-0.7201	-0.3330
log [F([OIII]5007)/F(H β)]	0.1549	-1.5031	-0.9790	-0.0297	–
log [F([OIII]5007)/F([OII]3727)]	-0.2839	-1.3881	-0.3172	–	–
log [F([OII]3727)/F(H β)]	0.5603	0.0450	-1.8017	-1.8434	-0.6549
log [F([OIII]5007)/F([NII]6584)]	0.4520	-2.6096	-0.7170	0.1347	–
log [F([NeIII]3870)/F([OII]3727)]	-1.2608	-1.0861	-0.1470	–	–

Notes: ^a R₂₃ = (F([OII]3727) + F([OIII]4959) + F([OIII]5007))/F(H β)

Table 5. Best fit parameters for analytical form of the mass-metallicity relation in Eq. 2 at different redshifts

z	$\log M_0$	K_0
0.07	11.18	9.04
0.7	11.57	9.04
2.2	12.38	8.99
3.5 ^a	12.76	8.79
3.5 ^b	12.87	8.90

Notes: ^a Value obtained by using the masses estimated with the BC03 templates. ^b Value obtained by using the masses estimated with the M05 templates.